PHYSICAL REVIEW A **92**, 032115 (2015)

Vacuum high-harmonic generation in the shock regime

P. Böhl,[1,*] B. King,[2,†] and H. Ruhl[1,‡]

[1]*Arnold Sommerfeld Center for Theoretical Physics, Ludwig-Maximilians-Universität München, Theresienstraße 37, 80333 München, Germany*

[2]*Centre for Mathematical Sciences, Plymouth University, Plymouth PL4 8AA, United Kingdom*

(Received 24 March 2015; published 11 September 2015)

Electrodynamics becomes nonlinear and permits the self-interaction of fields when the quantized nature of vacuum states is taken into account. The effect on a plane probe pulse propagating through a stronger constant crossed background is calculated using numerical simulation and by analytically solving the corresponding wave equation. The electromagnetic shock resulting from vacuum high-harmonic generation is investigated and a nonlinear shock parameter identified.

DOI: 10.1103/PhysRevA.92.032115 PACS number(s): 12.20.−m, 03.50.De, 03.65.Pm, 97.60.Jd

I. INTRODUCTION

Soon after the formulation of relativistic quantum mechanics, it became clear that the propagation of light through the vacuum would be modified due to the polarizability of virtual electron-positron pairs [1–4]. Heisenberg and Euler derived the Lagrangian of an effective description of this interaction for constant fields [5], which was later rederived by Schwinger [6]. Derivative expansions of this effective interaction [7–9] and numerical worldline calculations [10] imply that "constant" is to be taken with respect to the Compton time h/mc^2 for electron mass m. This suggests a good approximation of the effect for time-dependent fields with a much longer period than the Compton time is to simply insert them in place of the constant fields in the Heisenberg-Euler Lagrangian. In particular, the polarized vacuum supports the phenomenon of self-interaction when two electromagnetic waves couple via virtual electron-positron pairs and the principle of superposition no longer holds.

There have been several studies of the consequences of this self-interaction. Lutzky and Toll [11] showed that if the field invariant $\mathcal{G} = -FF^*/4E_{\rm cr}^2 = \mathbf{E}\cdot\mathbf{B} = 0$, where F, F^* are the Faraday tensor and its dual, $E_{\rm cr} = m^2c^3/\hbar e = 1.3\times10^{16}\,\mathrm{V\,cm^{-1}}$ is the so-called "critical" field, $e>0$ is the charge of a positron, and $\mathbf{E}$ and $\mathbf{B}$ are the total electric and magnetic fields in units of the critical field, a current that depends nonlinearly on the invariant $\mathcal{F} = -F^2/4E_{\rm cr}^2 = (E^2-B^2)/2$ leads to the generation of an electromagnetic discontinuity or "shock." After identifying an application in magnetized neutron stars, shocks were analyzed in a constant magnetic field background using a first- [12], second- [13], and several-order [14,15] weak-field expansion of the Heisenberg-Euler Lagrangian with an all-order analysis performed by Bialynicka-Birula [16]. An astrophysical environment was further modeled by introducing nonlinear vacuum effects into equations of relativistic magnetohydrodynamics [15] and into a dusty plasma [17].

In the current article we analyze a pump-probe setup of having a linearly polarized oscillating plane wave (probe) counterpropagate through a linearly polarized constant crossed and stronger plane wave background (pump). Of particular interest will be the two cases of having parallel or perpendicular probe and pump polarizations. Observables are expressed in terms of the electric and magnetic fields to aid comparison with numerical simulation.

Unlike in classical electrodynamics where a superposition of solutions to the wave equation is also a solution, when the existence of charged virtual electron-positron vacuum states is included, the principle of superposition is no longer valid. A consequence of using the Heisenberg-Euler Lagrangian is that a nontrivial vacuum "current" appears in Maxwell's equations, which disappears in the classical limit $\hbar\to0$. If the electromagnetic fields are not very weak $E \gg \sqrt{\alpha}(\hbar\omega/mc^2)^2$ [18], where $\alpha\approx1/137$ is the fine-structure constant and the field frequency is ω (corresponding to an intensity much greater than $10^5\,\mathrm{W\,cm^{-2}}$ for an optical laser), they can be regarded as classical. When this is the case, the methods of classical electrodynamics can be used to solve Maxwell's equations with the vacuum current.

For fields much weaker than critical, the interaction with the virtual electron-positron pairs of the vacuum permits $2n$-wave mixing for integer $n>1$ such as four- and six-wave mixing, as demonstrated in Fig. 1. One can make an analogy with nonlinear optics, in which the polarization $\mathbf{P}$ of an optical material can depend upon higher powers of the electric field [19], which are described using different orders of the susceptibility tensor $\chi^{(j)}$:

$$P_i = \chi^{(1)}_{ij}E_j + \chi^{(2)}_{ijk}E_jE_k + \cdots, \tag{1}$$

and analogously for the magnetization $\mathbf{M}$. Being a relativistic effect however, the magnetic and the electric fields appear in the vacuum polarization and magnetization on an equal footing. For weak fields and propagation lengths shorter than the scattering length, four-wave mixing is the most probable vacuum polarization process for colliding plane waves (with the exception of certain special field geometries). This is often compared to the optical Kerr effect [20], but in a pump-probe experiment in which the probe oscillates much quicker than the pump field, the steepening of the carrier wave [21] and not the envelope [22] is stronger.

If the fields' space time extent is much larger than a single scattering length, multiple $2n$-wave mixing can occur,

*patrick.boehl@physik.uni-muenchen.de
†b.king@plymouth.ac.uk
‡hartmut.ruhl@physik.uni-muenchen.de

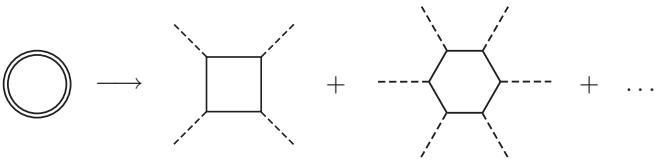

FIG. 1. An illustration of the weak-field expansion of the vacuum polarization diagram.

in which the change in field due to wave mixing influences further changes due to wave mixing, with each mixing event involving a potentially different n. Usually it is assumed that the probability for multiple mixing events is much lower than single mixing events, and multiple events are neglected. However, if the extent of the field is large enough, this hierarchy can be broken and it can become more probable that multiple mixing events occur than a single mixing event so that all orders of wave mixing events have to be taken into account. With the generation of a large number of higher harmonics, the shape of the electromagnetic plane waves will also change and this leads to the possibility of shock wave generation. In the "shock regime", as all orders of wave mixing can play a role in the generation of the spectrum, the spectrum is expected to be qualitatively different to the perturbative case of having only a single mixing event, where four-wave mixing is the most probable and higher harmonics are exponentially suppressed. Such a type of shock generation is also known from nonlinear optics [23].

In contrast to this, the weak-field expansion in Fig. 1 suggests that high-harmonic generation can also occur through single scattering events that involve large numbers of photons. The likelihood of this happening increases with the field strength of slowly varying weak fields. This type of *vacuum high-harmonic generation* has been investigated using the full polarization operator in [24,25] and using the lowest order of the weak-field expansion in [26–29]. A highlight of the current article is an investigation of vacuum high-harmonic generation in plane wave fields in what we call the *shock regime*, where the probe propagation length is much larger than the mean scattering length. It will be shown that in certain parameter regimes this can be a much more efficient high-harmonic generation mechanism.

The aims of this work are: (i) to investigate vacuum high-harmonic generation in the collision of plane waves that are weaker than critical, for the case that the fields' space time extent is much larger than the mean scattering length; (ii) to show that the higher harmonics are accompanied by an electromagnetic shock due to the polarized vacuum; (iii) to investigate the dependency of this shock on the colliding fields' mutual linear polarization; and (iv) to comment on the similarities and differences of high-harmonic generation in laser-irradiated plasmas.

We begin with a derivation of the modified Maxwell and wave equations (Sec. II), summarize the analytical method (Sec. III) and the numerical method used in computational simulation (Sec. IV) before analyzing higher harmonic generation with just four-wave mixing (Sec. V), just six-wave mixing (Sec. VI), and both four- and six-wave mixing (Sec. VII). We then discuss the results, compare with high-harmonic generation from oscillating plasmas (Sec. VIII), and conclude (Sec. IX).

II. MODIFIED ELECTROMAGNETIC WAVE PROPAGATION

The Heisenberg-Euler Lagrangian can be written [6,30]

$$\mathcal{L}_{\rm HE} = -\frac{m^4}{8\pi^2}\int_0^\infty ds\,\frac{e^{-s}}{s^3}\left[s^2 ab\cot as\coth bs - 1 + \frac{s^2}{3}(a^2-b^2)\right] \tag{2}$$

(we have set here and throughout $\hbar = c = 1$ unless they explicitly occur), where the secular invariants a and b are given by

$$a = [\sqrt{\mathcal{F}^2+\mathcal{G}^2}+\mathcal{F}]^{1/2}, \quad b = [\sqrt{\mathcal{F}^2+\mathcal{G}^2}-\mathcal{F}]^{1/2},$$

and we recall that electric and magnetic fields are in units of the critical field $E_{\rm cr}$. Applying the Euler-Lagrange equations to $\mathcal{L} = \mathcal{L}_{\rm MW} + \mathcal{L}_{\rm HE}$, where $\mathcal{L}_{\rm MW} = m^4(E^2-B^2)/8\pi\alpha$ is the classical Maxwell Lagrangian, gives the modified Maxwell equations:

$$\partial_\mu F^{*\mu\nu} = 0, \tag{3}$$

$$(1+C_1)\,\partial_\mu F^{\mu\nu} + C_2\,F^{\mu\nu}\partial_\mu F^2 + C_3\,F^{*\mu\nu}\partial_\mu(FF^*) + C_4\,[F^{*\mu\nu}\partial_\mu F^2 + F^{\mu\nu}\partial_\mu(FF^*)] = 0, \tag{4}$$

and the general expressions for the coefficients C_i are given in Appendix A. Expressing these equations in electric and magnetic fields, we acquire

$$\nabla\wedge\mathbf{E} + \partial_t\mathbf{B} = 0, \tag{5}$$

$$\nabla\wedge\mathbf{B} - \partial_t\mathbf{E} = \mathbf{J}[\mathbf{E},\mathbf{B}], \tag{6}$$

$$\mathbf{J}[\mathbf{E},\mathbf{B}] = [C_1(\partial_t\mathbf{E} - \nabla\wedge\mathbf{B}) + (C_2\mathbf{E}+C_4\mathbf{B})\partial_t F^2 + (C_2\mathbf{B}-C_4\mathbf{E})\wedge\nabla F^2 + (C_4\mathbf{B}-C_3\mathbf{E})\wedge\nabla(FF^*) + (C_3\mathbf{B}+C_4\mathbf{E})\partial_t(FF^*)]. \tag{7}$$

We restrict our analysis to the case when $E \ll 1$, for two reasons. First, it allows us to neglect the creation of real electron-positron pairs, as the probability of vacuum pair production in a volume equal to the reduced Compton wavelength $\lambda\!\!\!^{-} = \hbar/mc$ cubed in the Compton time $\lambda\!\!\!^{-}/c$ is $P = E^2\exp(-\pi/E)/4\pi^3$ [6], which is heavily suppressed for $E \ll 1$. Second, it permits a perturbative expansion in E, the so-called "weak-field expansion", of the Heisenberg-Euler Lagrangian.

Although all electromagnetic fields are classical, it is useful to envisage the corresponding quantum process involving photons and this is depicted for the weak-field expansion of the vacuum polarization operator in Fig. 1. (Indeed, it has been shown that the leading-order term of the weak-field expansion agrees with the direct calculation of the four-photon box diagram in the low-frequency limit $\hbar\omega \ll mc^2$ [31].) The

weak-field expansion of Eq. (2) for $E \ll 1$ is then

$$\mathcal{L}_{\rm HE} = \frac{m^4}{\alpha}\sum_{i=1}^{\infty}\mathcal{L}_i, \tag{8}$$

$$\mathcal{L}_1 = \frac{\mu_1}{4\pi}[(E^2-B^2)^2 + 7(\mathbf{E}\cdot\mathbf{B})^2], \tag{9}$$

$$\mathcal{L}_2 = \frac{\mu_2}{4\pi}(E^2-B^2)[2(E^2-B^2)^2 + 13(\mathbf{E}\cdot\mathbf{B})^2], \tag{10}$$

$$\mathcal{L}_3 = \frac{\mu_3}{4\pi}[3(E^2-B^2)^4 + 22(E^2-B^2)^2(\mathbf{E}\cdot\mathbf{B})^2 + 19(\mathbf{E}\cdot\mathbf{B})^4], \tag{11}$$

where $\mu_1 = \alpha/90\pi$, $\mu_2 = \alpha/315\pi$, $\mu_3 = 4\alpha/945\pi$ [although α occurs in the denominator in Eq. (8), as fields are in units of the critical field, when $\hbar \to 0$, $\mathcal{L}_{\rm HE} \to 0$]. The coefficients C_i in Eq. (4) that follow from $\mathcal{L}_1$ and $\mathcal{L}_2$ are given by Eqs. (A5)–(A10) in Appendix A.

In the scenario we consider, the initial electric field is $\mathbf{E}^{(0)}(\varphi_p,\varphi_s) = \mathbf{E}_p^{(0)}(\varphi_p) + \mathbf{E}_s^{(0)}(\varphi_s)$ and the initial probe and strong electric waves are given by

$$\mathbf{E}_p^{(0)}(\varphi_p) = \boldsymbol{\varepsilon}_p\,\mathcal{E}_p\,e^{-(\frac{\varphi_p}{\Phi_p})^2}\cos\varphi_p, \tag{12}$$

$$\mathbf{E}_s^{(0)}(\varphi_s) = \boldsymbol{\varepsilon}_s\,\mathcal{E}_s\,\mathrm{Rect}\left(\frac{\varphi_s}{\Phi_s}\right), \tag{13}$$

where the rectangular function $\mathrm{Rect}(\varphi/\Phi) = \theta(\varphi+\Phi/2) - \theta(\varphi-\Phi/2)$ and $\theta(\cdot)$ is the Heaviside function [32], $\varphi_p = k_p x = \omega_p x^-$, $\varphi_s = k_s x = \omega_s x^+$, $x^\pm = t \pm z$, $\Phi_p = \omega_p\tau_p$, $\Phi_s = \omega_s\tau_s$ with the probe and strong field polarization vectors $\boldsymbol{\varepsilon}_p, \boldsymbol{\varepsilon}_s$ obeying $\boldsymbol{\varepsilon}_p\cdot\boldsymbol{\varepsilon}_p = 1$, $\boldsymbol{\varepsilon}_s\cdot\boldsymbol{\varepsilon}_s = 1$, $\mathbf{k}_p\cdot\boldsymbol{\varepsilon}_p = 0$, $\mathbf{k}_s\cdot\boldsymbol{\varepsilon}_s = 0$ and the probe pulse is assumed to be much weaker than the strong background $\mathcal{E}_p \ll \mathcal{E}_s$. Initially, the probe and strong fields are well separated: $\lim_{t\to-\infty}\mathcal{F},\mathcal{G} = 0$. We define the orthonormal polarization vectors $(\boldsymbol{\varepsilon}^\parallel,\boldsymbol{\varepsilon}^\perp)$, where $\boldsymbol{\varepsilon}^\parallel \equiv \boldsymbol{\varepsilon}_p$ defines "parallel" polarization, and $\boldsymbol{\varepsilon}^\perp$ "perpendicular" polarization with $\boldsymbol{\varepsilon}^\perp\cdot\boldsymbol{\varepsilon}^\parallel = 0$, $\boldsymbol{\varepsilon}^\perp\cdot\mathbf{k}_p = 0$.

Since the vacuum current is a function of the relativistic invariants $\mathcal{F} = (E^2-B^2)/2$ and $\mathcal{G} = \mathbf{E}\cdot\mathbf{B}$, for single plane waves, there is no effect on propagation due to vacuum polarization [6,33,34]. Therefore, the only contributions will come from cross terms between the probe and strong field. As the weak-field expansion is an expansion in powers of $\mathcal{F}$ and $\mathcal{G}$, for our scenario, each order scales as $\mathcal{L}_n \sim (E_s E_p)^{n+1}$.

The initial probe $\mathbf{E}_p^{(0)}$ and strong $\mathbf{E}_s^{(0)}$ fields satisfy the classical vacuum wave equation independently:

$$\Box\,\mathbf{E}_p^{(0)} = \mathbf{0}, \quad \Box\,\mathbf{E}_s^{(0)} = \mathbf{0},$$

where $\Box = c^{-2}\partial_t^2 - \nabla^2$. The effect of the polarized vacuum can be included with a source term $\mathbf{T} = \mathbf{T}[\mathbf{E},\mathbf{B}]$ occurring on the right-hand side of the wave equation. The source is related to the current $\mathbf{J}$ in Maxwell's equations via $\mathbf{T} = \partial_t\mathbf{J}$. We will assume that solutions to this equation are also plane waves propagating along the same axis as the pump and probe waves. This allows us to write $\mathbf{T} = \mathbf{T}[\mathbf{E}]$. Since a single plane wave cannot polarize the vacuum [33,34]:

$$\mathbf{T}[\mathbf{E}_p] = \mathbf{0}, \quad \mathbf{T}[\mathbf{E}_s] = \mathbf{0}.$$

However, since two counterpropagating plane waves *can* polarize the vacuum, the wave equation we will solve is

$$\Box\,(\mathbf{E}_p + \mathbf{E}_s) = \mathbf{T}[\mathbf{E}_p + \mathbf{E}_s]. \tag{14}$$

In particular, we are interested in solutions which include the self-action of the probe that lead to a plasmalike vacuum instability and corresponding electromagnetic shock. Equation (14) will be solved in two ways. First, the scattered probe will be solved for using an analytical method based on an iterative procedure that ignores changes to the stronger background:

$$\Box\,\mathbf{E}_p^{(n+1)} = \mathbf{T}\big[\mathbf{E}_p^{(n)} + \mathbf{E}_s^{(0)}\big]. \tag{15}$$

Second, Eq. (14) will be solved consistently in a numerical simulation that uses tools based on the pseudocharacteristic method of lines, which are applied to the corresponding Maxwell equations. In this way, the "asymptotic" state of the probe field after it has passed through the strong field and $\mathbf{T} \approx \mathbf{0}$ (in contrast to the "overlap" dynamics when $\mathbf{T} \neq \mathbf{0}$ [28]) will be studied.

As we are considering the collision of counterpropagating plane waves, the general Maxwell's equations in Eqs. (5) and (6) reduce to one spatial (z) and one temporal (t) dimension. To determine which terms in the full weak-field expansion for the current Eq. (8) should be considered when calculating high-harmonic generation, we employ the following scaling argument. As explained in [28], the change in the field due to interaction with the vacuum that propagates with the probe ("forward" scattering) is

$$\Delta\mathbf{E}_p(x^-) = \int_{-\infty}^{z}\frac{dz'}{2}\mathbf{J}(t' = x^- + z', z'), \tag{16}$$

where the vacuum current is

$$\mathbf{J} = \sum_{i=1}^{\infty}\mathbf{J}_i, \quad \mathbf{J}_i = 4\pi[\widehat{\mathbf{k}}_p\wedge\partial_z\mathbf{M}_i + \partial_t\mathbf{P}_i]. \tag{17}$$

$\widehat{\mathbf{k}}_p = \mathbf{k}_p/|\mathbf{k}_p|$ and the dimensionless vacuum polarization $\mathbf{P}_i = \partial\mathcal{L}_i/\partial\mathbf{E}$ and magnetization $\mathbf{M}_i = \partial\mathcal{L}_i/\partial\mathbf{B}$ (as used in, e.g., [16] or [35]). The forward-scattered signal is zero if the vectorial part of $\mathbf{P}_i$ or $\mathbf{M}_i$ is from the probe field. As already explained, $\mathcal{L}_n \sim (E_s E_p)^{n+1}$, but in the wave equation that results from this, the vacuum current contains derivatives with respect to E_s and E_p. Since the current containing the derivative with respect to E_s vanishes in the asymptotic signal for forward scattering in plane waves [28,36], we see that the remaining current and hence the scattered field $J_n \propto \mu_n\mathcal{E}_s^{n+1}\mathcal{E}_p^n$. The integration over z' is over the strong field and so contributes a factor τ_s and the differentials in Eq. (17) contribute approximately a factor ω_p, so that one can estimate $\Delta E_p^{(1)} \propto \mu_n\mathcal{E}_s^{n+1}\mathcal{E}_p^n\Phi$, for $\Phi = \omega_p\tau_s$. Since we assume $E \ll 1$, and since we are interested in the case when the change in the probe is of the same order as the probe field and self-interaction becomes important, we require $\Phi \gg 1$. We also note that the coefficients μ_n diverge with n because the weak-field expansion is asymptotic (see, e.g., [37]), so we do not expect the series can be truncated for arbitrarily large n and still yield a useful approximation. Although purely four-photon

scattering does allow the generation of higher harmonics in this setup, this first occurs for double four-photon scattering. The contribution from this twice-iterated process appears in $\Delta\mathbf{E}_p^{(2)}$ and scales as $\propto(\mu_1)^2\mathcal{E}_s^3\mathcal{E}_p^2\Phi$, which when compared to the leading contribution to second harmonic generation from six-photon scattering in $\Delta E_p^{(1)} \propto \mu_2\mathcal{E}_s^3\mathcal{E}_p^2\Phi$, is suppressed by a factor $(\mu_1)^2/\mu_2 \ll 1$. Therefore, when considering higher harmonic generation along the probe propagation axis in the regime $E \ll 1$, $\Phi \gg 1$, the leading contribution originates from six-photon scattering. In Sec. V this simple scaling argument will be seen to agree with the full numerical analysis. An argument for neglecting eight-photon scattering will be forthcoming.

III. ANALYTICAL METHOD

To solve the inhomogeneous wave equation

$$\left[\partial_t^2 - \partial_z^2\right]\mathbf{E}_p = \mathbf{T}\left[\mathbf{E}_p + \mathbf{E}_s^{(0)}\right], \tag{18}$$

we employ an iterative ansatz:

$$\mathbf{E}_p^{(n+1)} = \mathbf{E}_p^{(0)} + \Delta\mathbf{E}_p^{(n)}, \tag{19}$$

where

$$\Delta\mathbf{E}_p^{(n)}(t,z) = \int dt'\,dz' G(t-t',z-z')\mathbf{T}^{(n)}(t',z'),$$

and in general

$$\mathbf{T}^{(n)}(t,z) = \sum_{i=1}^{\infty}\mathbf{T}_i\left[\mathbf{E}_p^{(n-1)}(\varphi_p) + \mathbf{E}_s^{(0)}(\varphi_s)\right],$$

where the subscript i is the order of the weak-field expansion and the retarded Green's function is [38]

$$G(t,z) = \frac{\mathsf{n}}{2}\theta(t)\theta\left(\frac{t}{\mathsf{n}} - |z|\right),$$

for refractive index n. If $\mathsf{n} = 1$, one acquires Eq. (16), where $\partial_t\mathbf{J}^{(n)}(t,z) = \mathbf{T}^{(n)}(t,z)$. These equations can be iterated to calculate the generation of higher harmonics due to multiple scattering as outlined in the section Introduction. Within this analytical approach, we assume $\omega_p\tau_p \gg 1$ and $\omega_p\tau_s \gg 1$, so that the derivative of the probe and background envelopes can be neglected with respect to the derivative of the oscillating part of the probe in $\mathbf{J}$. When studying the generation of higher harmonics, we will be particularly interested in taking

$$\mathbf{T}^{(n)}(t,z) = \mathbf{T}_2\left[\mathbf{E}_p^{(n-1)}(\varphi_p) + \mathbf{E}_s^{(0)}(\varphi_s)\right],$$

which corresponds to considering purely six-photon scattering (this will be further justified shortly).

A diagrammatic approach is useful to understand the physical processes described by different iterations of the probe field $\mathbf{E}_p^{(n)}$. First, since we are interested in harmonic generation and since the background is constant, we suppress strong-field photon legs. Furthermore, as the Heisenberg-Euler Lagrangian is "effective" in that all fermion dynamics have been integrated out, all vacuum loops are reduced to effective vertices. Then the diagram representing six-photon scattering, which is the leading order harmonic-generating process, is given in Fig. 2. The iterative ansatz in Eq. (19) is illustrated in Table I.

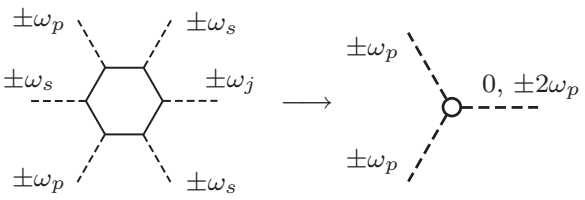

FIG. 2. In the left-hand diagram, $\omega_j \in \{\omega_s, 3\omega_s, 2\omega_p \pm \omega_s, 2\omega_p \pm 3\omega_s\}$. If the strong field is approximated as constant and the three strong-field photon legs are suppressed, in an effective approach, six-photon scattering of the probe can be represented as a triple interaction. The ± refer to incoming and outgoing photons respectively.

The diagrammatic equation in Table I in some ways resembles the Schwinger-Dyson equation [39] but in this case the left-hand side is the self-consistent solution of the probe field at a particular order of iteration, and the double line on the right-hand side is where the scattered probe field from the previous order is applied. In Table I it is shown how the number of diagrams rapidly increases with iteration order (as the square of the number in the previous order plus one, although many are equivalent). It also demonstrates that terms of a much higher perturbative order (number of vertices) are generated at a given iterative order [$\mathbf{E}^{(n)}$ contains terms from the $(2^n - 1)$th perturbative order, but is only accurate to the nth perturbation order].

On all the diagrams with at least one vertex, one leg is the scattered field and the rest are incoming or outgoing probe photons. An example is given in Fig. 3 where the ± sign refers to the energy added to the system by incoming

TABLE I. Diagrammatic representation of the first iterations of the probe wave equation.

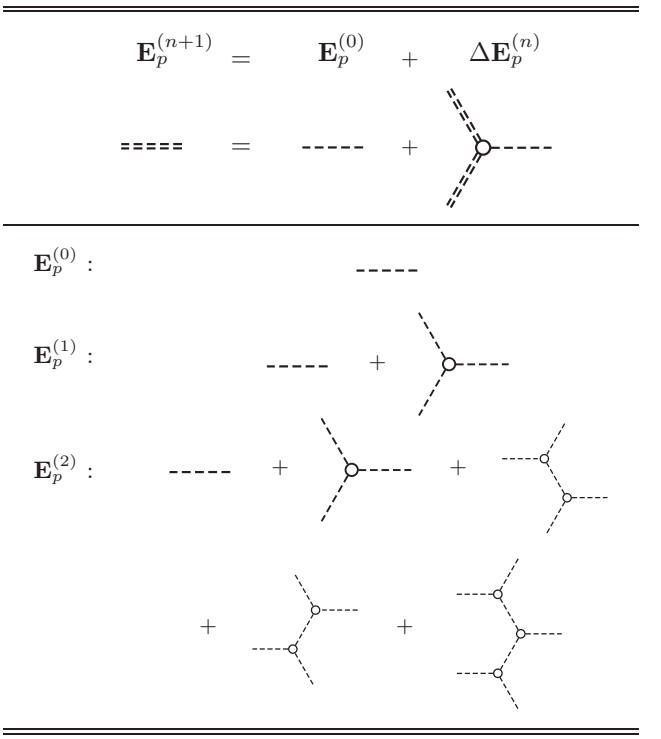

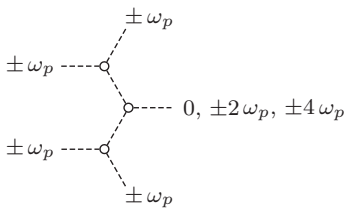

FIG. 3. An example of the harmonics generated in the probe due to effective self-interaction in a slowly varying background.

and outgoing photons respectively. By summing the series that occurs in $\lim_{n\to\infty}\mathbf{E}_p^{(n)}$, we will arrive at an analytical expression for the asymptotic probe field and in doing so identify a shock parameter that signifies when self-action effects become important.

For the example of parallel probe and strong field polarization, the second iteration shown in Table I is

$$\mathbf{E}_p^{(2)} = \boldsymbol{\varepsilon}_p\,\mathcal{E}_p e^{-(\frac{\varphi_p}{\Phi_p})^2}\Big[\Big(1-\Big(\frac{v}{2}\Big)^2 g^{(11)}(\varphi_s)\Big)\cos\varphi_p - \frac{v}{2}g^{(1)}(\varphi_s)\sin 2\varphi_p - 3\Big(\frac{v}{2}\Big)^2 g^{(11)}(\varphi_s)\cos 3\varphi_p + 2\Big(\frac{v}{2}\Big)^3 g^{(2)}(\varphi_s)\sin 4\varphi_p\Big], \tag{20}$$

where $v=\nu_2\exp[-(\varphi_p/\Phi_p)^2]$ and the shock parameter $\nu_2 = 192\mu_2\mathcal{E}_s^3\mathcal{E}_p\Phi$. The functions of φ_s describe how the particular term is generated *during* the passage of the probe through the strong background (all fields are classical) and originate from repeated integration of the interaction over coordinate. Here

$$g^{(1)}(\varphi_s) = \int_{-\infty}^{\varphi_s/\Phi_s} dy\,\mathrm{Rect}\,(y),$$
$$g^{(11)}(\varphi_s) = \int_{-\infty}^{\varphi_s/\Phi_s} dy\,\mathrm{Rect}\,(y)g^{(1)}(y), \tag{21}$$
$$g^{(2)}(\varphi_s) = \int_{-\infty}^{\varphi_s/\Phi_s} dy\,\mathrm{Rect}\,(y)\,[g^{(1)}(y)]^2,$$

and these are plotted in Fig. 4.

As mentioned in the section Introduction, we are mainly interested in the *asymptotic* state of the probe:

$$\mathbf{E}_p^{(2)}(\varphi_p) = \lim_{\varphi_s\to\infty}\mathbf{E}_p^{(2)}(\varphi_p,\varphi_s), \tag{22}$$

where we note $\lim_{\varphi_s\to\infty} g^{(1)}(\varphi_s)=1$, $\lim_{\varphi_s\to\infty} g^{(11)}(\varphi_s)=1/2$, and $\lim_{\varphi_s\to\infty} g^{(2)}(\varphi_s)=1/3$.

As previously remarked, using this method, $\mathbf{E}_p^{(n)}$ contains powers of v from 0 to 2^n-1 but is only accurate to $O(v^n)$. We also note that the nth iteration generates harmonics from 1 to 2^n. A power series in v multiplies each harmonic so we can write a given iteration as

$$\mathbf{E}_p^{(n)}(\varphi_p,\varphi_s) = \boldsymbol{\varepsilon}_p\,\mathcal{E}_p e^{-(\frac{\varphi_p}{\Phi_p})^2}\sum_{j=1}^{\infty}\big[a_{2j}^{(n)}(v,\varphi_s)\sin 2j\varphi_p + a_{2j-1}^{(n)}(v,\varphi_s)\cos(2j-1)\varphi_p\big]. \tag{23}$$

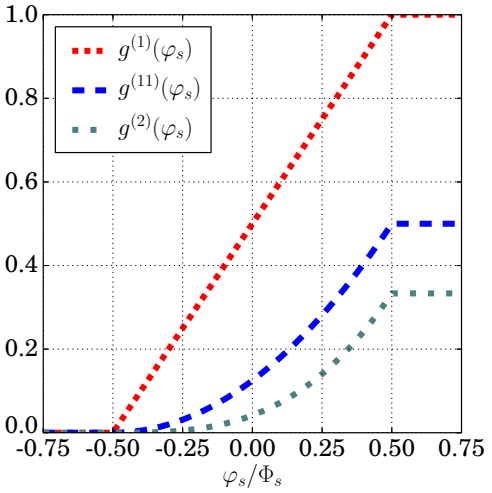

FIG. 4. (Color online) A plot of how the functions describing how the occurrence of higher harmonics varies with probe propagation length.

Of most interest is the asymptotic state of the full solution:

$$\mathbf{E}_p(\varphi_p) = \lim_{\varphi_s\to\infty}\lim_{n\to\infty}\mathbf{E}_p^{(n)}(\varphi_p,\varphi_s),$$

and we find that for the parallel setup:

$$\lim_{\varphi_s\to\infty}\lim_{n\to\infty} a_j^{(n)}(v,\varphi_s) = a_j(v) = 2(-1)^{\lfloor j/2\rfloor}\frac{J_j(jv)}{jv}, \tag{24}$$

where $\lfloor j\rfloor=\mathrm{floor}(j)$ and $J_l(\cdot)$ is the lth-order Bessel function of the first kind [40]. We note that the all-order solution Eq. (24) for a plane probe propagating through a constant crossed, parallel-polarized background, resembles the Fubini solution [41] for the propagation of lossless finite-amplitude planar acoustic waves in nonlinear media [42].

The all-order solution can be derived from a probe-dependent refractive index: $\mathsf{n}=1+\delta\mathsf{n}_2$ with $\nu_2=\delta\mathsf{n}_2\Phi$ where

$$\delta\mathsf{n}_2(\varphi_s,\varphi_p) = 192\mu_2 E_s^3(\varphi_s)E_p(\varphi_p). \tag{25}$$

So the scattered probe field due to just six-photon scattering can be written:

$$\mathbf{E}_p(\varphi_p) = \mathbf{E}_p^{(0)}(\varphi_p+\nu_2[E_p(\varphi_p)]). \tag{26}$$

To justify when it is a good approximation to only consider six-photon scattering, let us consider first eight-photon scattering. The shock parameter for eight-photon scattering is $\nu_3 = 1536\mu_3\mathcal{E}_s^4\mathcal{E}_p^2\Phi$. In order that this is much less than ν_2, we require $\mathcal{E}_s\mathcal{E}_p \ll 3/32$, and since $\mathcal{E}_s \ll 1$ and $\mathcal{E}_p \ll 1$, this is fulfilled. Therefore, the individual effect of the next higher-order terms in the weak-field expansion should be negligible. In contrast, the importance of four-photon scattering can be quantified by the parameter $\nu_1 = 16\mu_1\mathcal{E}_s^2\Phi$ but this corresponds to the process of one incoming and one outgoing photon from a scattering event and therefore will not contribute directly to harmonic generation. Nevertheless, it does lead to a refractive index alteration, which in combination with multiple six-photon scattering, could potentially influence the generated spectrum. To ignore this in our analysis would

require $\mathcal{E}_s\mathcal{E}_p \gg 7/24$, which is not fulfilled. To explore this point, the simulation results are split into three cases: (i) purely four-photon scattering, (ii) purely six-photon scattering, and (iii) both four- and six-photon scattering. We consider two polarization scenarios: the "parallel setup" and the "perpendicular setup", which refer to the initial strong field polarization being in the $\boldsymbol{\varepsilon}^{\parallel}$ and $\boldsymbol{\varepsilon}^{\perp}$ mode, respectively. In the parallel setup, we will find all harmonics are generated in the parallel polarization mode $\boldsymbol{\varepsilon}^{\parallel}$, whereas for the perpendicular setup, each odd harmonic will be generated in a perpendicular mode $\boldsymbol{\varepsilon}^{\perp}$ and each even harmonic in a parallel one $\boldsymbol{\varepsilon}^{\parallel}$.

IV. NUMERICAL METHOD

For the scenario of two colliding plane wave pulses, the modified Maxwell equations in Eqs. (5) and (6) can be written in matrix form

$$(\mathbb{1}_4 + \mathbf{X})\partial_t \mathbf{f} + (\mathbf{Q} + \mathbf{Y})\partial_z \mathbf{f} = 0, \tag{27}$$

where $\mathbf{f} = (E_x, E_y, B_x, B_y)^T$, $\mathbb{1}_4$ is the identity matrix in four dimensions, $\mathbf{Q} = \mathrm{adiag}(1,-1,-1,1)$ is an antidiagonal matrix, and $\mathbf{X}$ and $\mathbf{Y}$ are the perturbations due to vacuum interaction given in a general form in Appendix B.

Our numerical method, which was first employed by the authors in [28] and will be explained in more detail in the following, is based on inverting the matrix $(\mathbb{1}_4 + \mathbf{X})$ to convert Eq. (27) to a system of ordinary differential equations (ODEs), discretizing in space using the "pseudocharacteristic method of lines" (PCMOL) [43] and integrating the equations of motion using the ODE solver CVODE [44].

Our analysis is valid when $\mathcal{E}_s, \mathcal{E}_p \ll 1$ and the single parameter relevant to high-harmonic generation in the shock regime that depends on the field strength is $\nu_2 = 192\mu_2\mathcal{E}_s^3\mathcal{E}_p\Phi$. We wish to simulate the occurrence of a shock wave, for which $\nu_2 \to 1$, implying Φ must be very large in order to compensate for the weak field strengths. However, a large Φ is computational expensive to simulate. To compare analytical and numerical results, we will therefore extrapolate the theoretical result to values of $\mathcal{E}_s \not\ll 1$, allowing a simulation for smaller Φ to be performed, with the condition that the physical prediction is only valid for a particular value of ν_2 when $\mathcal{E}_s \ll 1$. For this reason, we will often quote simulation parameters in terms of shock parameters rather than absolute field strengths and spatial extensions.

A. Linear case

Let us first consider (27) with $\mathbf{X} = \mathbf{Y} = \mathbf{0}$, which is the $\hbar \to 0$ limit. This system is hyperbolic [45], which means that we can find a basis $\mathbf{u} := \mathbf{S}\,\mathbf{f}$ such that the matrix $\boldsymbol{\Lambda} = \mathbf{S}\mathbf{Q}\mathbf{S}^{-1} = \mathrm{diag}(-1,-1,1,1)$ is diagonal with real eigenvalues:

$$\mathbf{S} = \frac{1}{\sqrt{2}}\begin{pmatrix} -1 & 0 & 0 & 1 \\ 0 & 1 & 1 & 0 \\ 1 & 0 & 0 & 1 \\ 0 & -1 & 1 & 0 \end{pmatrix}, \quad \mathbf{u} := \mathbf{S}\,\mathbf{f} = \frac{1}{\sqrt{2}}\begin{pmatrix} B_y - E_x \\ E_y + B_x \\ E_x + B_y \\ B_x - E_y \end{pmatrix}. \tag{28}$$

In this new basis we have an uncoupled system of advection equations:

$$\partial_t \mathbf{u}(t,z) + \boldsymbol{\Lambda}\,\partial_z \mathbf{u}(t,z) = 0.$$

The diagonal elements λ_i of $\boldsymbol{\Lambda}$ are called the "characteristic speeds" of the system, where $\lambda_i = \pm 1$ corresponds to a component traveling along the characteristics $x^{\pm}$ with the speed of light. We proceed by introducing a co-located grid for the components u_i with N grid points. The field components u_i on the grid are arranged blockwise in a large $4N$-dimensional vector $\tilde{\mathbf{u}} = (\cdots u_4^{l-1} u_1^l u_2^l u_3^l u_4^l u_1^{l+1} \cdots)$, where $u_i^l = u_i(l\Delta z)$ and $0 < l \leqslant N$ is the index of the grid point. The PCMOL uses biased differencing for each component u_i according to the sign of the corresponding characteristic speed λ_i, where the component u_i with $\lambda_i > 0$ ($\lambda_i < 0$) is thereby differentiated using backward (forward) finite differences using fourth-order accuracy. In [46] it is argued that this biased differencing using five-point-stencils is an effective fixed grid method for first order hyperbolic partial differential equations because it shows a good balance between introducing minimal numerical diffusion and oscillations in the solution where steep gradients are present. The derivatives at the boundary are also approximated using only field values inside the box. Instead of transforming the system back to $\tilde{\mathbf{f}}$ (the tilde in this section indicates the discretized version on the grid), which is normally done in the PCMOL, the system is solved for $\tilde{\mathbf{u}}$. This has the advantage of having open boundary conditions since the components u_i are only allowed to flow in one direction. If we take the system to be of size L and a spatial resolution of N grid points, then distance is measured in units of $\Delta z = L/(N-1)$, where $N-1$ corresponds to the boundary conditions being taken into account. We are left with a system of ODEs $\tilde{\mathbf{u}}'(t) = \mathbf{g}[\tilde{\mathbf{u}}(t),t]$, where $\mathbf{g}[\tilde{\mathbf{u}}(t),t] = -\tilde{\boldsymbol{\Lambda}}\,\mathbf{D}\,\tilde{\mathbf{u}}$, with the 4×4 matrix $\boldsymbol{\Lambda}$ being mapped onto a $4N \times 4N$ dimensional block-diagonal one, $\tilde{\boldsymbol{\Lambda}} = \mathbb{1}_N \otimes \boldsymbol{\Lambda}$ ($\otimes$ is the Kronecker product [47]) and $\mathbf{D}$ being the $4N \times 4N$ matrix representing the biased differencing explained above. For the detailed action of $\mathbf{D}$ on $\tilde{\mathbf{u}}$ see Appendix C.

The initial conditions are set up in $\tilde{\mathbf{f}}$, the system is integrated in $\tilde{\mathbf{u}}$ using CVODE and transformed back for output. CVODE is an ODE solver that offers variable-order, variable-step multistep methods. Initially we supply the "right-hand-side function" $\mathbf{g}[\tilde{\mathbf{u}}(t),t]$ as above. Since both the linear and nonlinear cases are nonstiff (no rapidly damped modes are expected), we apply the Adams-Moulton methods together with the variational method to solve the resulting linear system. This provides higher accuracy with less computational effort compared to the offered Newton iterations, since neither approximations nor an analytical expression for the Jacobian have to be provided. We always use the parallel implementation of CVODE together with "extended" (long double) precision.

B. Nonlinear case

By discretizing the full nonlinear system (27), the matrices $\mathbf{X}$ and $\mathbf{Y}$ also become $4N \times 4N$ dimensional. The system then can also be brought into ODE form $\tilde{\mathbf{u}}'(t) = \mathbf{g}[\tilde{\mathbf{u}}(t),t]$ by inverting the matrix $(\mathbb{1}_{4N} + \tilde{\mathbf{X}})$. Since $\mathbf{X}$ depends only on the field components, the full matrix can be written as $\tilde{\mathbf{X}} = \oplus_{l=1}^{N} \mathbf{X}^l$

($\oplus$ is the direct sum [47]) and the upper index denotes the former 4×4 matrix $\mathbf{X}$ at grid point l. This can be used to reduce the inversion of $\tilde{\mathbf{X}}$ to N times the inversion of a 4×4 matrix. The structure of $\mathbf{X}^l$ allows us to rewrite $\mathbf{X}^l$ as $\mathbf{X}^l = \mathbf{G}\,\mathbf{H}^l$ with

$$\mathbf{G} = \begin{pmatrix} 1 & 0 \\ 0 & 1 \\ 0 & 0 \\ 0 & 0 \end{pmatrix}, \quad \mathbf{H}^l = \begin{pmatrix} x^l_{11} & x^l_{12} & x^l_{13} & x^l_{14} \\ x^l_{21} & x^l_{22} & x^l_{23} & x^l_{24} \end{pmatrix},$$

where the x^l_{ij} are the values of the nonvanishing matrix elements of $\mathbf{X}$ given in Appendix B, evaluated at position l. Then we can apply the Woodbury formula [48]

$$(\mathbb{1}_4 + \mathbf{X}^l)^{-1} = \mathbb{1}_4 - \mathbf{G}(\mathbb{1}_2 + \mathbf{H}^l\mathbf{G})^{-1}\mathbf{H}^l\,,$$

to further reduce the inversion to one of the 2×2 matrix

$$(\mathbb{1}_2 + \mathbf{H}^l\mathbf{G}) = \begin{pmatrix} 1 + x^l_{11} & x^l_{12} \\ x^l_{21} & 1 + x^l_{22} \end{pmatrix}.$$

This is performed for all grid points using an LU factorization at each evaluation of the function $\mathbf{g}[\tilde{\mathbf{u}}(t),t]$.

For the parameters considered, the nonlinear corrections $\mathbf{X}$ and $\mathbf{Y}$ do not change the signs of the characteristic speeds, so we use the same biased differencing as in the linear case. The nonlinear ODE system is then given by

$$\tilde{\mathbf{u}}'(t) = -\tilde{\mathbf{S}}(\mathbb{1}_{4N} + \tilde{\mathbf{X}})^{-1}(\tilde{\mathbf{Q}} + \tilde{\mathbf{Y}})\tilde{\mathbf{S}}^{-1}\mathbf{D}\,\tilde{\mathbf{u}},$$

where $\tilde{\mathbf{S}} = \mathbb{1}_N \otimes \mathbf{S}$, $\tilde{\mathbf{Q}} = \mathbb{1}_N \otimes \mathbf{Q}$, and $\tilde{\mathbf{Y}} = \oplus_{l=1}^{N} \mathbf{Y}^l$ in analogy to $\tilde{\mathbf{X}}$. All fields are normalized by $E_{\rm cr}$. The parameters for CVODE are the same as in the linear case. The signals are analyzed under the assumption $\omega = |\mathbf{k}|$ using a spatial Fourier transform in *Wolfram Mathematica* [49].

C. Simulational setup

Recalling the form of the probe and strong pulses [Eqs. (12) and (13)], we consider a Gaussian probe pulse with base frequency ω_p and a "constant" strong pulse. We consider the two cases of parallel and perpendicular setups which are characterized by parallel and perpendicular polarizations, respectively, of the probe and the strong pulse with $\boldsymbol{\varepsilon}_p \cdot \boldsymbol{\varepsilon}_s = 1$ and $\boldsymbol{\varepsilon}_p \cdot \boldsymbol{\varepsilon}_s = 0$. The rectangular shape of the strong pulse is approximated using a mirrored Fermi-Dirac distribution in the simulation box. The function FD(y) is given by

$$\mathrm{FD}(y) = \frac{1}{1 + \exp\left(\frac{|y| - \omega_s z_m}{\omega_s z_b}\right)}\,. \tag{29}$$

The parameters z_b and z_m play the role of the "temperature" and "chemical potential," controlling the steepness and width of the strong pulse. Typical values are $z_b = 5 \times 10^{-5}$ cm and $z_m = 100 \cdot z_b$.

A snapshot of the simulation box for $t = 0$ is shown in Fig. 5. The use of a Fermi-Dirac distribution instead of a Rect function follows the advice in [46], where it is recommended to avoid sharp gradients (which is infinite for a Rect function) because of numerical diffusion and spurious oscillations. To ensure the accuracy of the simulations, we use a sufficiently high number of grid points for the Fermi-Dirac function and generated shock waves in order to resolve the gradients properly so that spurious effects are suppressed.

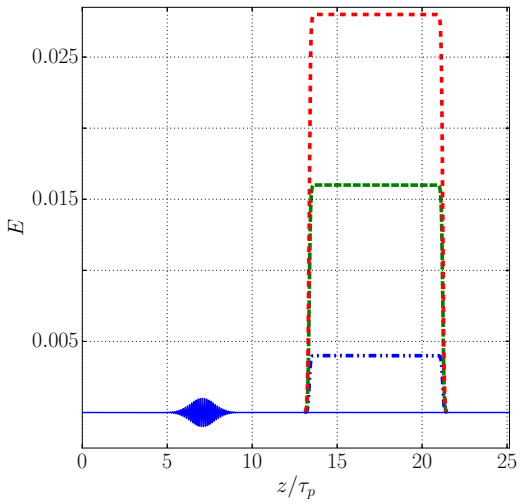

FIG. 5. (Color online) The simulational setup for the collision of a Gaussian probe pulse with a constant pulse of various strengths (indicated by different line styles) and identical polarization. The size of the system is taken to be 3.2×10^{-2} cm.

The initial conditions are

$$\begin{aligned} \mathbf{E}_p(\phi_p,\phi_{0p}) &= \boldsymbol{\varepsilon}_p \mathcal{E}_p\, e^{-\frac{(\phi_p - \phi_{0p})^2}{\Phi_p}} \cos(\phi_p - \phi_{0p}), \\ \mathbf{E}_s(\phi_s,\phi_{0s}) &= \boldsymbol{\varepsilon}_s \mathcal{E}_s \mathrm{Rect}[(\phi_s - \phi_{0s})/\Phi_s] \\ &\approx \boldsymbol{\varepsilon}_s \mathcal{E}_s \mathrm{FD}(\phi_s - \phi_{0s}), \\ \mathbf{B}_i(\phi_i,\phi_{0i}) &= \widehat{\mathbf{k}}_i \wedge \mathbf{E}_i(\phi_i,\phi_{0i}), \end{aligned}$$

with $\phi_i = \omega_i z$, $\phi_{0i} = \omega_i z_{0i}$, $\Phi_i = \omega_i \tau_i$, and $i \in \{p,s\}$.

To define the pulse duration τ_s of the strong pulse when using the Fermi-Dirac function, we equate the calculation of the first iteration for the simulational parallel setup with the analytical model [see Eqs. (16) and (21)]:

$$\begin{aligned} \Delta\mathbf{E}^{(1)}_p(\varphi_p) &= \lim_{\varphi_s \to \infty} -\boldsymbol{\varepsilon}_s \mathcal{E}_p e^{-(\frac{\varphi_p}{\Phi_p})^2} \frac{v}{2} \frac{h^{(1)}(\varphi_s)}{\tau_s} \sin 2\varphi_p \\ &= -\boldsymbol{\varepsilon}_s \mathcal{E}_p e^{-\left(\frac{\varphi_p}{\Phi_p}\right)^2} \frac{v}{2} \sin 2\varphi_p, \end{aligned}$$

where $h^{(1)}(\varphi_s)$ is given by

$$h^{(1)}(\varphi_s) = \frac{1}{\omega_s} \int_{-\infty}^{\varphi_s} dy\, \mathrm{FD}^3(y).$$

The duration τ_s is then defined by $\tau_s = \lim_{\varphi_s \to \infty} h^{(1)}(\varphi_s)$. The initial conditions are chosen such that the field invariants and the field values at the boundary are essentially zero initially and the system is simulated until the pulses are again well separated.

Results of the simulation were compared to the analytical result for asymptotic lowest order second harmonic generation in the parallel and perpendicular setups [28], where the Gaussian strong background in [28] is replaced with the mirrored Fermi-Dirac distribution Eq. (29). The excellent agreement is displayed in Fig. 6, where the log-log plot of the ratio $I(2\omega_p)/I^{(0)}_p(\omega_p)$ for various values of the strong field

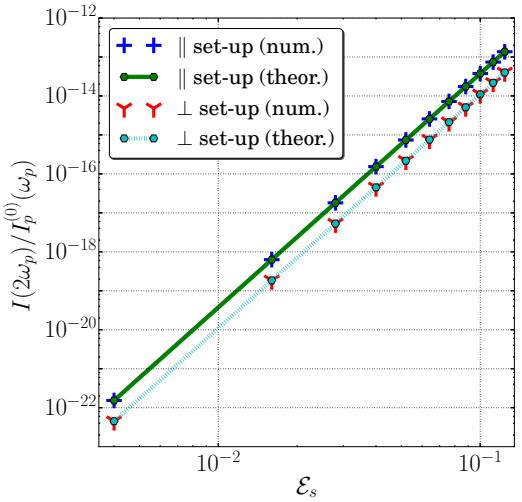

FIG. 6. (Color online) The relative intensity of the second harmonic generated by single six-photon scattering for $\mathcal{E}_p = 10^{-3}$.

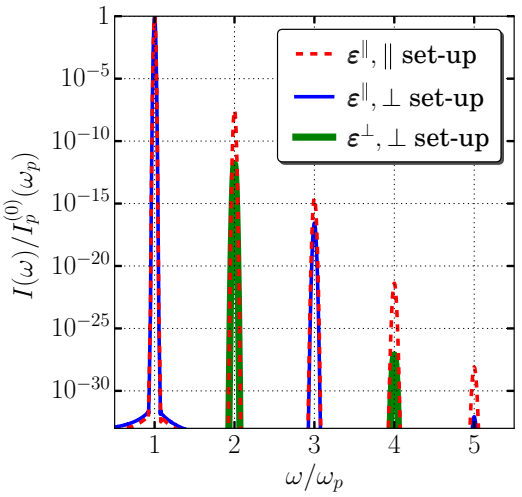

FIG. 7. (Color online) High-harmonic generation from multiple four-photon scattering for $\upsilon_1 = 3.3 \times 10^{-4}$.

amplitude is calculated using

$$\frac{I(\omega)}{I_p^{(0)}(\omega_p)} = \left[\frac{|\widetilde{E}_p(\omega)|}{|\widetilde{E}_p^{(0)}(\omega_p)|}\right]^2, \quad \widetilde{\mathbf{E}}_p(\omega) = \int_{-\infty}^{\infty} dx^- \mathbf{E}_p(x^-)\, e^{i\omega x^-}. \tag{30}$$

V. ALL-ORDER FOUR-PHOTON SCATTERING

For the parameter regime of interest, the most probable effect on the probe pulse due to four-photon scattering is that from the well-studied modified vacuum indices of refraction $\mathsf{n}_1^{\parallel,\perp} = 1 + \delta\mathsf{n}_1^{\parallel,\perp}$ given by [50,51]

$$\delta\mathsf{n}_1^{\parallel,\perp} = 2(11 \mp 3)\mu_1 \mathcal{E}_s^2, \tag{31}$$

which can be written in a phase-dependent way $\mathsf{n}_1(\varphi_s) = 1 + \delta\mathsf{n}_1(\varphi_s)$:

$$\delta\mathsf{n}_1(\varphi_s) = 4\mu_1 \left[E_s^{(0)}(\varphi_s)\right]^2 [4(\boldsymbol{\varepsilon}_p \cdot \boldsymbol{\varepsilon}_s)^2 + 7(\boldsymbol{\varepsilon}_p \wedge \boldsymbol{\varepsilon}_s)^2]. \tag{32}$$

Following the analytical method in Sec. III, summing all perturbative orders, one finds due to purely four-photon scattering [corresponding to using $\mathbf{T} = \mathbf{T}_1$ in Eq. (18)], in the parallel setup:

$$\mathbf{E}_p(\varphi_p) = \sum_{j=0}^{\infty} \frac{\upsilon_1^j}{j!} \frac{d^j}{d\varphi_p^j} \mathbf{E}_p^{(0)}(\varphi_p) = e^{\upsilon_1 \frac{d}{d\varphi_p}} \mathbf{E}_p^{(0)}(\varphi_p),$$

which is just a shift operator in the phase that is applied to the initial probe pulse giving

$$\mathbf{E}_p(\varphi_p) = \mathbf{E}_p^{(0)}(\varphi_p + \upsilon_1),$$

where the multiscale parameter for the parallel and perpendicular cases $\upsilon_1 = \upsilon_1^{\parallel,\perp}$:

$$\upsilon_1^{\parallel,\perp} = 2(11 \mp 3)\mu_1 \mathcal{E}_s^2 \Phi = \delta\mathsf{n}_1^{\parallel,\perp} \Phi. \tag{33}$$

This all-order solution to the phase shift in a plane wave propagating through a constant background derived from the Heisenberg-Euler Lagrangian complements a recent example solution of the phase shift derived from the Schwinger-Dyson equation applied to the polarization operator [52].

Photon merging via single four-photon scattering is prohibited in a plane wave counterpropagating parallel to the background [28,36]. However, when the possibility of multiple four-photon scattering is taken into account, high-harmonic generation *can* take place. The modified refractive index Eq. (32), experienced by the probe due to the strong field and conversely the modified refractive index experienced by the strong field due to the probe, leads to the electromagnetic invariants $\mathcal{F}$, $\mathcal{G}$ no longer vanishing for the probe and strong fields separately. A log-log plot of the normalized spectrum $I(\omega)/I_p^{(0)}(\omega_p)$ for various cases of high-harmonic generation through purely four-photon scattering is displayed in Fig. 7.

The perpendicular setup leads to even harmonics being generated in the $\boldsymbol{\varepsilon}^{\parallel}$ mode and odd harmonics being generated in the $\boldsymbol{\varepsilon}^{\perp}$ mode. All higher harmonics in the perpendicular setup are suppressed compared to the parallel setup, with odd harmonics being suppressed more than even ones. In the parallel setup, all photons are scattered into the $\boldsymbol{\varepsilon}^{\parallel}$ mode. As will become clear in Sec. VI, compared to the six-photon channel, harmonic generation via four-photon scattering is considerably suppressed. The scaling argument given at the end of Sec. III can now be understood in the following way. For purely four-photon scattering, one scattering event must have occurred to change the electromagnetic variants (a factor $\delta\mathsf{n}_1 = 16\mu_1\mathcal{E}_s^2$) and one further scattering with a probe photon (a factor $\upsilon_1 = 16\mu_1\mathcal{E}_s\mathcal{E}_p\Phi$), which yields the combination

$$\upsilon_1 = (16\mu_1)^2 \mathcal{E}_s^3 \mathcal{E}_p \Phi. \tag{34}$$

If one takes this to be the shock parameter for purely four-photon scattering, for the parameters of the parallel setup in Fig. 7, following Eq. (20), one would expect the second harmonic at relative intensity $(\upsilon_1/2)^2 = 10^{-7.6}$, third harmonic at $(3\upsilon_1^2/8)^2 = 10^{-14.8}$, and the fourth harmonic at $(\upsilon_1^3/12)^2 = 10^{-23.0}$, which correctly predict the numerical

results to within an order of magnitude. For comparison, the shock parameter for purely six-photon scattering for this setup would be $\nu_2 = 2.7 \gg \nu_1$.

VI. ALL-ORDER SIX-PHOTON SCATTERING

As already hinted, six-photon scattering is the dominant process in the generation of higher harmonics for $E \ll 1$ in the plane wave setup we are considering. For this reason we choose here to analyze six-photon scattering as the single vacuum interaction. Many of the features of the following harmonic spectra will be common to the combined four- and six-photon scattering case in Sec. VII.

The parameter $\upsilon_2 = \nu_2 \exp[-(\varphi_p/\Phi_p)^2]$ is bounded by $\upsilon_2 \leqslant \nu_2$, so the different behavior of the scattered probe will be quantified using the shock parameter ν_2. As ν_2 is increased from zero, two regimes become apparent: (i) the perturbative regime $\nu_2 \ll 1$, where the occurrence of higher harmonics is exponentially suppressed; and (ii) the shock regime, where the intensity of the jth harmonic is proportional to a power-law $j^{\gamma(\upsilon)}$, with $\gamma(\upsilon) < -2$.

To highlight the nature of the harmonic generation surrounding shock formation, we refer in the following to the parallel setup for simplicity, and discuss differences in the perpendicular setup in Sec. VI C.

In Fig. 8 are log-log plots of three different types of normalized spectrum $I(\omega)/I_p^{(0)}(\omega_p)$ in the parallel setup. In the first panel (a) $\nu_2 = 0.05 \ll 1$ and the perturbative regime can be recognized by the exponential suppression of higher harmonics. In the middle panel (b) $\nu_2 = 0.6$ and a transition regime can be identified in which the lower harmonics are no longer exponentially suppressed but obey a power-law behavior and the leading-order perturbative expansion is inaccurate for higher harmonics. In the final panel (c) $\nu_2 = 1$ and the entire plotted spectrum has a power-law behavior, distinctive of the shock regime, in which an all-order expansion is required to even reach a correct qualitative conclusion. Since we are considering only six-photon scattering, we set $\nu_2 = \nu$ and $\upsilon_2 = \upsilon$ in the following discussion.

A. Perturbative regime

If $\nu \ll 1$, the amplitude of each harmonic in the scattered electric field is

$$|a_j(\nu)| = \frac{1}{\Gamma(1+j)}\left(\frac{\nu j}{2}\right)^{j-1} + O(\nu^{j+1}). \tag{35}$$

For $\nu j \ll 1$ but $j \gg 1$, using Stirling's approximation [53] $\Gamma(1+j) \approx \sqrt{2\pi j}(j/e)^j$, we see

$$|a_j(\nu)| = \frac{(\nu e)^j}{\nu j^{3/2}\sqrt{2\pi}}, \qquad \left|\frac{a_{j+1}(\nu)}{a_j(\nu)}\right| \approx \nu e, \tag{36}$$

and the exponential dependency of each harmonic becomes manifest. In the first panel of Fig. 8, the dots denote the intensities of the harmonics when only the leading perturbative order is taken into account. The excellent agreement is typical of the perturbative regime, in which only a small proportion of probe photons have scattered, and double scattering is much less probable than single scattering. In the transition regime, the leading-order terms of the perturbative expansion overestimate the intensity of the higher harmonics. In the shock regime, the leading-order perturbation terms both qualitatively and quantitatively disagree with the numerical solution and all-order analytical solution.

B. Shock regime

In this regime, ν no longer fulfills $\nu \ll 1$ and all orders of the perturbative expansion must be summed in order to calculate the spectrum of generated harmonics. This is demonstrated in the third panel of Fig. 8 which shows excellent agreement between the numerical and analytical solution Eqs. (23) and (24). We note that even though the all-orders solution includes the phase-dependent parameter $\upsilon = \nu \exp[-(\varphi_p/\Phi_p)^2]$, we can still arrive at a qualitative understanding of this regime by considering the effect on the probe pulse at the point $\varphi_p = 0$. In this case, $\upsilon = \nu$ and the relative amplitude of consecutive harmonics is

$$\left|\frac{a_{j+1}(\nu)}{a_j(\nu)}\right| = \left|\frac{J_{j+1}[(j+1)\nu]}{J_j(j\nu)}\right| \frac{j}{j+1}. \tag{37}$$

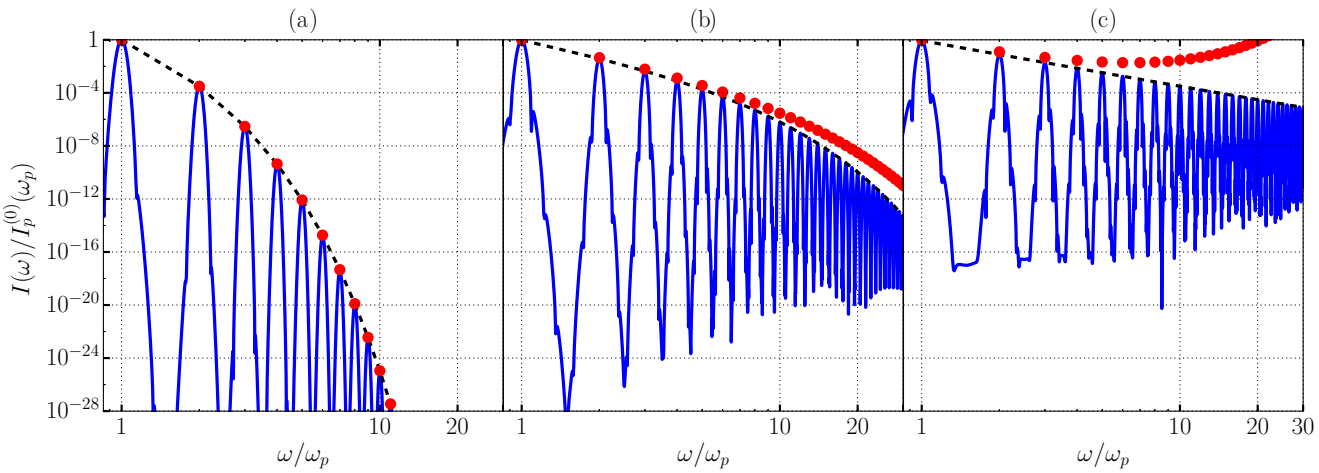

FIG. 8. (Color online) Harmonic spectra in the parallel setup for different regimes of solution: (a) $\nu_2 = 0.05$, (b) $\nu_2 = 0.6$, and (c) $\nu_2 = 1$. The dots show the leading-order perturbative term, the dashed line is the all-order analytical solution, and the solid line is from numerical simulation.

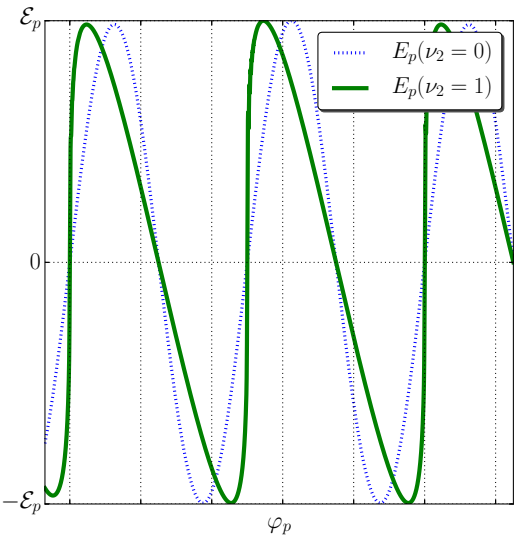

FIG. 9. (Color online) After passing through the polarized vacuum in the parallel setup, the probe pulse wave fronts can steepen significantly.

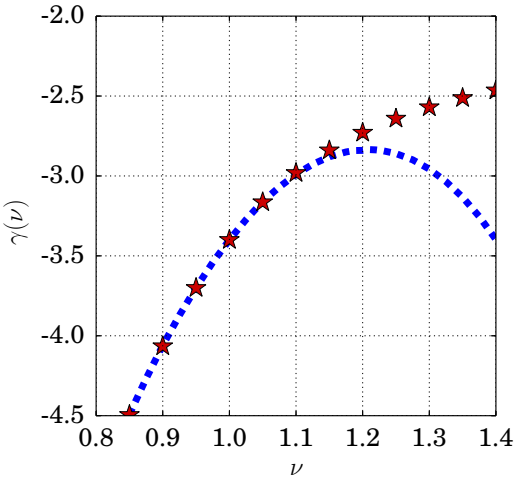

FIG. 10. (Color online) Comparison of the power-law exponent $\gamma(\nu)$ for different values of the shock parameter ν, as calculated using the fourth and tenth harmonics from the analytical (dashed line) and numerical (points) solutions.

Using the asymptotic form for $j\nu \to \infty$, $|J_j(j\nu)| \sim (2\pi j)^{-1/2}$ (when phase terms are neglected) [54], we see that for large enough argument, the ratio of harmonic amplitudes becomes

$$|a_j(\nu)| \sim \frac{1}{\nu\, j^{3/2}}\sqrt{\frac{2}{\pi}}, \quad \left|\frac{a_{j+1}(\nu)}{a_j(\nu)}\right| \sim \left(\frac{j}{j+1}\right)^{3/2}, \quad (38)$$

and the power-law behavior is manifest. For $\nu = 1$, this gives a ratio of the intensity of the jth harmonic to the initial probe intensity, $I_p^{(j)}(\varphi_p)/I_p^{(0)}(\varphi_p) = [E_p^{(j)}(\varphi_p)/E_p^{(0)}(\varphi_p)]^2$ of

$$\log_{10}\left(\frac{I_p^{(j)}(\varphi_p = 0)}{I_p^{(0)}(\varphi_p = 0)}\right) \underset{j\nu\to\infty}{\sim} -\log_{10}\frac{2}{\pi} - 3\log_{10} j. \quad (39)$$

The predicted gradient of $\gamma = -3$ should be an overestimate because $v < \nu$ for all parts of the probe apart from at $\varphi_p = 0$. In fact, the full result in the third panel of Fig. 8 yields $\gamma = -3.4$.

A plot of the scattered probe field and induced electromagnetic shock is displayed in Fig. 9. Those parts of the probe field that are positive and have a larger amplitude are decelerated more than those that are positive with a smaller amplitude. Where the field is positive, this leads to a steepening behind the peaks. Those parts of the probe that are negative but have a larger amplitude are decelerated less than those that are negative but have a smaller amplitude, hence leading to a steepening in the opposite direction where the field is negative. The result is the development of a sawtooth wave form shown in Fig. 9, which is typical of a second-order susceptibility [55].

The coefficient of the jth harmonic is weighted with the Bessel function $J_j(j\nu)$. When v is small, $J_j(j\nu)$ is a rapidly decaying function of j so higher harmonics are strongly suppressed. As $v \to 1^-$, the decay becomes much shallower. So a simplified picture of what type of shock is generated for the scenario explored in this paper can be made by setting the Bessel function to a constant. In the parallel setup, a discontinuous electric field with a backwards-leaning wave form of the form Fig. 9 is generated with

$$\mathbf{E}(\varphi) = \boldsymbol{\varepsilon}\mathcal{E}\sum_{j=1}^{\infty}(-1)^j\left[\frac{\cos(2j-1)\varphi}{2j-1} + \frac{\sin 2j\varphi}{2j}\right], \quad (40)$$

with polarization $\boldsymbol{\varepsilon}$ and amplitude $\mathcal{E}$, and the corresponding intensity spectrum has a power law $\sim j^{-2}$ for harmonic j. Indeed we find on a plot of $\gamma(\nu)$ (see Fig. 10), that as ν increases above 1, the power-law exponent in the numerical spectrum increases, tending toward a theoretical maximum of -2, at which point the lack of a unique solution to Maxwell's equations would halt further propagation of the probe. For $\nu > 1$, the numerical spectrum displays a variable power law, which is shallower for higher harmonics where the agreement with the analytical solution Eqs. (23) and (24) becomes increasingly worse. The power-law exponent calculated using the fourth and tenth harmonic is displayed in Fig. 10, where unlike in the numerical solution, in which the spectrum becomes progressively shallower, the analytical solution reaches a maximum shallowness. It is unclear what physical mechanism would cause this maximum to occur, which suggests this is a limitation of the viability of the analytical solution. Indeed when $v > 1$ in the analytical solution, $J_j(j\nu)$ can oscillate with j, and the ordering of harmonics can become no longer monotonic.

As the numerical spectrum becomes shallower, very high harmonics appear, which questions the validity condition $j\omega_p \ll m$ for using the Heisenberg-Euler Lagrangian to describe the vacuum interaction, and questions how steep the power law can become before relaxation processes would take over.

C. Polarization dependency

The previous sections are for the parallel setup. For the perpendicular setup, even harmonics are generated in the parallel mode $\boldsymbol{\varepsilon}^{\parallel}$ and odd harmonics in the perpendicular mode $\boldsymbol{\varepsilon}^{\perp}$. This is demonstrated in the spectrum in Fig. 11,

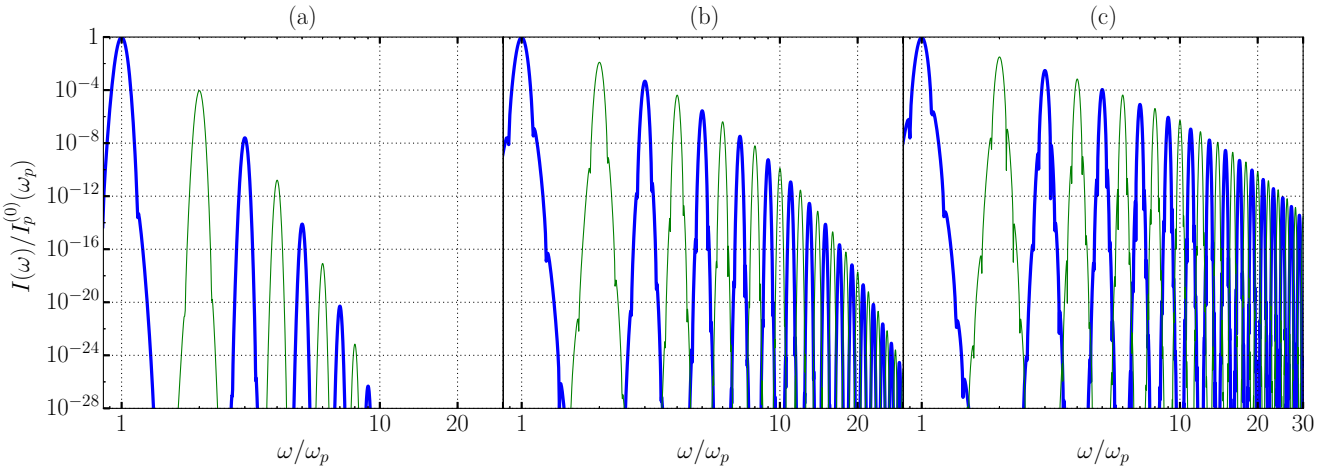

FIG. 11. (Color online) Harmonic spectra from numerical simulation of the perpendicular setup for different regimes of solution: (a) $\nu_2 = 0.05$, (b) $\nu_2 = 0.6$, and (c) $\nu_2 = 1$. The thick blue (thin green) peaks are harmonics parallel to the probe (strong) pulse.

where the thick and thin lines distinguish how the generated harmonics are polarized.

The shock wave generated in the perpendicular setup is displayed in Fig. 12. The scattered field in the $\boldsymbol{\varepsilon}^{\parallel}$ mode demonstrates a shock of a different nature to in the parallel setup, tending towards a square rather than a sawtooth wave form. Such a wave form can be generated with the sum

$$\mathbf{E}_{\text{square}}(\varphi) = \boldsymbol{\varepsilon}\mathcal{E}\sum_{j=1}^{\infty}(-1)^j\,\frac{\cos(2j-1)\varphi}{2j-1}, \tag{41}$$

which is just the odd frequencies of Eq. (40).

In the $\boldsymbol{\varepsilon}^{\perp}$ mode, a similar shock to in the parallel setup is seen, only with double the frequency. Such a sawtooth electric field is given by the sum [53]

$$\mathbf{E}_{\text{saw}}(\varphi) = \boldsymbol{\varepsilon}\mathcal{E}\sum_{j=1}^{\infty}(-1)^j\,\frac{\sin 2j\varphi}{2j}, \tag{42}$$

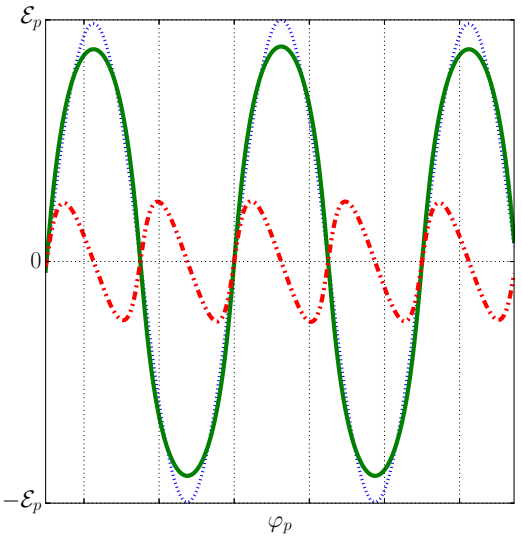

FIG. 12. (Color online) A probe that is initially polarized perpendicular to the background (blue dashed line) experiences different shocks in the $\boldsymbol{\varepsilon}^{\perp}$ (dot-dashed red line) and $\boldsymbol{\varepsilon}^{\parallel}$ (solid green line) modes.

which is just the even frequencies of Eq. (40), beginning at double the frequency of the seed probe field.

VII. ALL-ORDER FOUR- AND SIX-PHOTON SCATTERING

Although six-photon scattering is the most efficient process in generating high harmonics, for the parameter regime we are interested in, the effect of four-photon scattering as a modified vacuum refractive index cannot be neglected. Since the interaction with the vacuum includes powers of the probe field, the effects of phase lag and harmonic generation can mix in a highly nonlinear way. In this section we give the results of numerical simulations that include both processes.

For the parallel setup, the spectrum generated by six-photon scattering (for example, as shown in Fig. 8), is not visibly affected by the inclusion of four-photon scattering. However, for the perpendicular setup, since even and odd harmonics are in different polarization modes and since the vacuum is birefringent so each polarization mode experiences a different phase lag, the inclusion of four-photon scattering was found to increase the asymmetry between the even and odd harmonics compared with the purely six-photon scattering case. This is demonstrated in Fig. 13 for the case $\upsilon_1 = 100$, $\nu_2 = 1$, which compares the spectrum of harmonics generated when: (i) only four-photon scattering is included (left-hand panel); (ii) only six-photon scattering is included (middle panel), and (iii) four- and six-photon scattering are included (right-hand panel). The right-hand panel demonstrates the increased asymmetry between even and odd harmonics.

As the case of four- and six-photon scattering differs from the six-photon scattering case only for the perpendicular setup, we focus our discussion on this. Then there are three cases of interest: (i) weakly dispersive: $\upsilon_1 \ll \nu_2$; (ii) dispersive: $\upsilon_1 \approx \nu_2$; and (iii) strongly dispersive: $\upsilon_1 \gg \nu_2$. The first case of weak vacuum dispersion is within the parameter regime of interest, but outside of the regime that can be numerically simulated as it would require $\mu_2\Phi \gtrsim 0.1$ if the hierarchy $\mathcal{E}_s \gg \mathcal{E}_p$ were to be maintained. In the limit of vanishing dispersion, we expect the results from purely six-photon scattering case to be valid

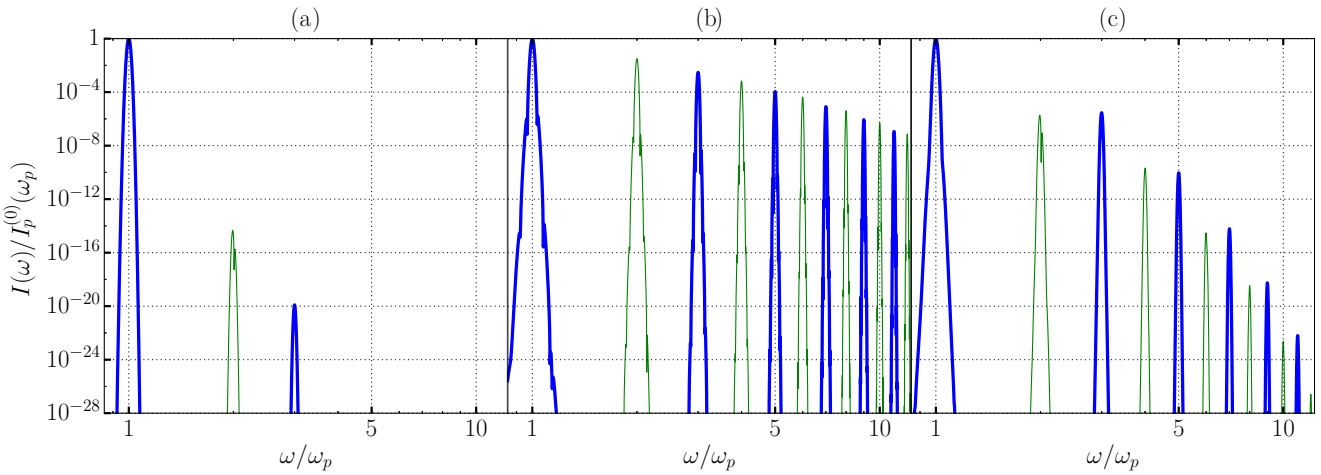

FIG. 13. (Color online) High-harmonic generation for the perpendicular setup when four- and six-photon scattering are present and four-photon scattering is much more prevalent than six-photon scattering ($\upsilon_1 = 100$, $\nu_2 = 1$). The first panel (a) is for just four-photon scattering, the second panel (b) for just six-photon scattering, and the third panel (c) for when both are present. The thick blue (thin green) peaks are again harmonics parallel to the probe (strong) pulse.

(this will be seen to be implied from the results of a dispersive vacuum).

A. Dispersive vacuum $\upsilon_1 \approx \nu_2$

When vacuum dispersion is significant, one might expect the nature of the shock wave to change. Two cases were simulated: (i) when $\upsilon_1 = \nu_2 = 1$ and (ii) when $\upsilon_1 = 5$, $\nu_2 = 1$. For the first case of equal parameters, the shock wave in Fig. 14 was generated. This bears a close resemblance to the shock wave generated in the perpendicular setup for a dispersionless vacuum ($\upsilon_1 \to 0$), i.e., when only six-photon scattering is present, but with a noticeable lag due to the now nonunitary refractive index. However, when the amount of dispersion is increased, setting $\upsilon_1 = 5$ and $\nu_2 = 1$, the shock wave takes on the different form shown in Fig. 15. In this dispersive case, the parallel mode develops a shock reminiscent of an optical Kerr medium, in which the polarization contains a cubic nonlinearity $P_i = \chi^{(1)}_{ij} E_j + \chi^{(3)}_{ijkl} E_j E_k E_l$. This is in some ways unsurprising because the parallel mode only contains odd harmonics and therefore odd powers of the field, and the largest nonlinear term originates from an E_p^3 term. Therefore, the symmetry of the scattered field when the field direction is swapped $\mathcal{E}_p \to -\mathcal{E}_p$ is different for the parallel field (which contains only even powers of $\mathcal{E}_p$) and the perpendicular field (which contains only odd powers of $\mathcal{E}_p$).

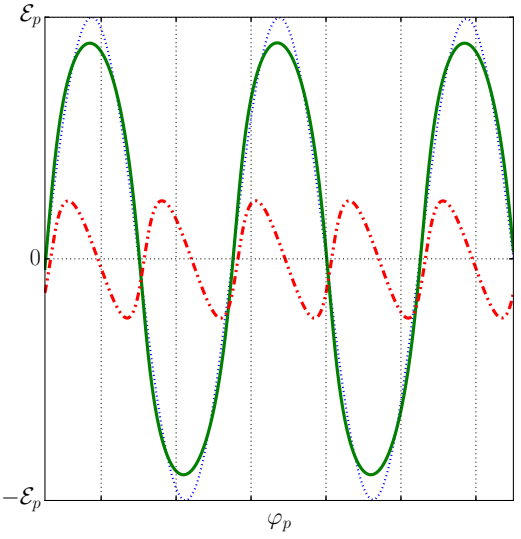

FIG. 14. (Color online) The weakly dispersive case for the perpendicular setup. The initially $\boldsymbol{\varepsilon}^{\parallel}$ polarized probe (blue dashed line) experiences the mixture of the probe-independent vacuum refractive index (here $\upsilon_1 = 1$) and the shock-inducing probe-dependent vacuum refractive index (here $\nu_2 = 1$). The $\boldsymbol{\varepsilon}^{\parallel}$ mode (dot-dashed red line) and $\boldsymbol{\varepsilon}^{\perp}$ mode (solid green line) behave differently.

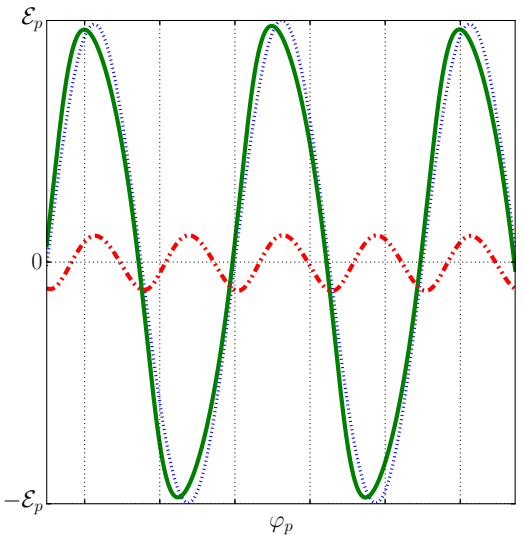

FIG. 15. (Color online) When the dispersion is increased ($\upsilon_1 = 5$, $\nu_2 = 1$), a different type of shock is formed in the $\boldsymbol{\varepsilon}^{\parallel}$ mode (dot-dashed red line) and the shock in the $\boldsymbol{\varepsilon}^{\perp}$ mode (solid green line) is reduced, where the initially $\boldsymbol{\varepsilon}^{\parallel}$ polarized probe is plotted by the blue dashed line.

Carrier-wave shocking also occurs in nonlinear optical materials. Our findings are similar to those reported in [56], where excellent agreement was obtained between theory and simulation in the dispersionless limit of a Kerr-like nonlinear material, but where it was noted how involved the analysis becomes if there is a complicated phase dependency between the generated harmonics. In the current work, in the parallel setup with dispersion (i.e., four- and six-photon scattering present), all harmonics experience the same refractive index so a shock wave can build up. In the perpendicular setup, the refractive index in the $\boldsymbol{\varepsilon}^{\perp}$ mode is different to in the $\boldsymbol{\varepsilon}^{\parallel}$ mode. We are studying a regime in which harmonics are generated by a chain of scattering processes. Since in each chain of processes that lead to the generation of a specific harmonic, the probe spends a different amount of time in the $\boldsymbol{\varepsilon}^{\perp}$ than in the $\boldsymbol{\varepsilon}^{\parallel}$ mode, the probability for each chain will be multiplied by a different phase. When the probability of all possible chains is summed over, it is reduced compared to the parallel setup due to each probability being added incoherently. This leads to a suppression of shock wave generation.

B. Strongly dispersive vacuum $\upsilon_1 \gg \nu_2$

To investigate shock wave generation in the strongly dispersive regime, we set $\upsilon_1 = 100$ and $\nu_2 = 1$. A new type of behavior becomes apparent, namely the deformation of the probe pulse envelope. The bandwidth of the probe is of the order $1/\tau_p$ but due to dispersive effects, frequencies of this magnitude can no longer be neglected. Since $\upsilon_1 = \delta\varphi_p = \omega_p T$, where T is the duration of propagation, frequencies from the probe envelope separated by $1/\tau_p$ will acquire a temporal separation relative to the duration of the pulse of $\upsilon_1/\omega_p\tau_p \ll 1$. Furthermore, the second harmonic is considerably suppressed when dispersion is included, such that it is of the same order of magnitude as the scattering of the probe envelope frequency. For this reason, the effect on the probe envelope can be seen so clearly in the $\boldsymbol{\varepsilon}^{\perp}$ component in Fig. 16.

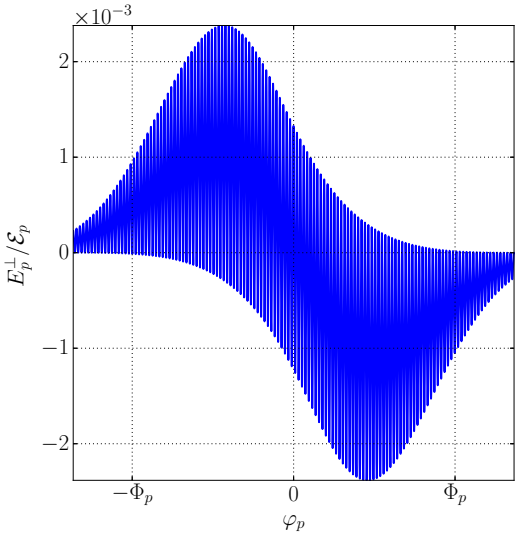

FIG. 16. (Color online) The probe pulse after having scattered in the strong background when $\upsilon_1 = 100$, $\nu_2 = 1$.

VIII. DISCUSSION

A. Comparison with high-harmonic generation in oscillating plasmas

There is a certain similarity between high-harmonic generation due to the relativistic movement of electrons in the plasma of laser-irradiated foil experiments and the virtual electron-positron "plasma" of the laser-irradiated vacuum. The vacuum is transparent when the invariants $E^2 - B^2$ and $\mathbf{E}\cdot\mathbf{B}$ are zero. Therefore, the vacuum is transparent to a pure plane wave and these invariants also typically remain much smaller for a single focused pulse than for counterpropagating pulses. So unlike with the plasma present in a foil, the vacuum plasma must first be "activated" by being polarized by some second "pump" pulse, similar to in a pump-probe experiment. In the current work, the vacuum was polarized by a background with the profile of a rectangular function. As the leading-order nonlinear polarization was proportional to the applied field cubed, it suggests that the local charge density is also nonzero in this region. The rectangular function is used to model the electron density in a solid before it is exposed to a laser pulse [57] and also to represent the laser's profile and in capillary discharge waveguides [58]. The difference with the vacuum is that the polarized material can in some way be "formed" by the pump pulse in the moment it is traversed by a probe.

For the parallel setup, all harmonics were generated in the parallel mode, but for the perpendicular setup odd harmonics were generated in the parallel mode with even harmonics in the perpendicular one. Just as in single nonlinear Compton scattering [59], the generation of the parallel mode is more probable than the perpendicular one. The relationship between polarization and harmonic order is reminiscent of selection rules for harmonics generated in laser-foil experiments, for example in the "p-polarized" (parallel to plane of incidence) and "s-polarized" (perpendicular to plane of incidence) harmonics in the widely used oscillating mirror model [60].

In the harmonic spectrum generated by a real plasma in laser-foil experiments, there is also a region of power-law decay and a region of exponential decay, as found here for vacuum high-harmonic generation. For the oscillating mirror model, power-law exponents of $\gamma = -5/2$ [61] and $\gamma = -8/3$ [62] have been postulated, and experiments on solid targets have recorded intensity-dependent power-law exponents, for example in [63] of $-5.50 < \gamma < -3.38$. These values are close to the analytical and numerical values found in the current work for vacuum high-harmonic generation in the shock regime $-4.5 \lesssim \gamma < -2$ (the lower limit corresponds to the gradient when the power-law behavior becomes manifest at $\nu_2 \approx 0.85$). Moreover, the power-law exponent $\gamma = \gamma(\nu_2)$ is also a function of the shock parameter $\nu_2 \propto \Phi$ and therefore increases with further propagation of the probe through the polarized vacuum, up to a theoretical maximum of $\gamma(\nu_2) < -2$. In contrast to the overdense plasma case, with our plane wave model and increasing shock parameter, we found no indication of a frequency cutoff, although at some frequency, pair-creation processes will play a role. By this we mean that higher harmonics can seed tunneling pair creation in the background field [64,65] or colliding photons with wave vectors k_1 and k_2 satisfying $k_1 k_2 \gtrsim 2m^2$ would lead to

multiphoton pair creation (the Breit-Wheeler process [66,67]). This would presumably deplete the higher harmonics that are directly related to the steepening of the wave fronts and act as a wave-breaking mechanism for the shock wave.

In the parallel setup, each harmonic has a regular phase relationship to the others and so a shock wave can build up as the amplitude of higher harmonics increases. In contrast to this, in the perpendicular setup, since there are many different chains of processes that can lead to the creation of a given harmonic, and since in each chain a different amount of time is spent in each polarization, which leads to different dispersion relations, the phase of each harmonic is related to the others in a nontrivial way and they are summed incoherently. This behavior is similar to that found in studies of nonlinear optical materials [56], and leads to the suppression of shock wave generation.

Although high-harmonic generation is present in laser-gas and laser-liquid experiments, the spectrum generated is of a completely different form. As harmonics are generated via the three-step recombination mechanism undergone by an electron in the Coulomb field of a nucleus, the electrons' trajectory and hence harmonics generated, are of a fundamentally different nature and demonstrate a genuine "plateau" region in spectra that is not present in vacuum high-harmonic generation as studied in the present work [68].

B. Validity of approach

By considering colliding plane waves, scattering in the transverse direction was ignored. One can estimate when this is a good approximation by defining the diffraction parameter $l = w^2/\lambda_p \tau_s$, where w is the width of the probe pulse in the transverse plane (assumed smaller than the width of the background). When $l \gg 1$ one is in the "near zone" and diffraction effects should be negligible, whereas $l \ll 1$ represents the "far zone" and diffraction effects become important [69].

The numerical simulation and analytical calculation predict a self-steeping of the probe wave fronts, which increases with shock parameter ν, until the wave fronts reach a theoretical maximum of becoming infinitely steep at which point the solutions to the wave equation are no longer unique. Since the Heisenberg-Euler Lagrangian is expected to be valid when the typical scale of a field inhomogeneity is much larger than the reduced Compton wavelength, this infinite steepening is not expected to be physically realizable. Moreover, no relaxation processes are included. If transverse dimensions would be taken into account, since six-photon scattering depends on the probe amplitude, self-focusing effects should be present. Furthermore, self-focusing can also occur via four-photon scattering as the probability for asymptotic second-harmonic generation via four-photon scattering becomes nonzero when the colliding probe photons do not propagate in parallel. So when transverse dimensions are included, as the probe propagates, it becomes less like a plane wave and the higher harmonics can seed real electron-positron pair creation as previously described.

The polarization of other vacuum virtual particle species such as muons, pions, and quarks was neglected, as the energy scale associated with these particles is much higher [70]. For that reason, we confined our discussion to the polarization of virtual electron-positron pairs.

C. Measurability

Vacuum high-harmonic generation in the shock regime becomes important when the shock parameter $\nu \approx 1$. Taking as an example six-photon scattering for the parallel setup $\nu = \nu_2 = 192\mu_2 \mathcal{E}_s^3 \mathcal{E}_p \Phi$. The current record for the highest electric field of a laser pulse produced in a laboratory [71] is of the order $3 \times 10^{-4} E_{\rm cr}$. Recalling that fields are written in units of the critical field, and that $\mu_2 = \alpha/315\pi \ll 1$, it is clear that the shock regime is currently well out of the reach of optical laser-based experiments. Vacuum polarization effects that can more likely be measured in laser-based experiments include elastic photon-photon scattering [29,72–83] or lowest-order photon merging [26,27,84,85]. (A review of strong-field QED effects can be found in [86,87].) The current best experimental limits for photon-photon scattering in an all-optical laser setup [88] and combining magnetic fields with resonant optical cavities [89,90] are still orders of magnitude above the QED prediction.

Where such vacuum electromagnetic shocks and accompanying harmonic generation might play a role, is in the evolution of x-ray pulsars and strongly magnetized neutron stars or "magnetars" [91–93]. Photons are emitted from the surface of such objects and propagate through magnetic fields of strength up to and beyond $E_{\rm cr}$ (in the system of units we use $B_{\rm cr} = E_{\rm cr}$), in plasmas of around 0.1–10 cm in depth [94]. The current results were derived for a constant crossed field background, but can be generalized to a constant magnetic field, which should be a good approximation to the local field in strongly magnetic pulsars, which is expected to be that of a dipole [94] on the stellar scale.

IX. CONCLUSION

When the quantum nature of the vacuum is taken into account, an electromagnetic shock accompanies high-harmonic generation in an oscillating plane probe pulse counterpropagating through a stronger slowly varying plane pulse. We have identified a nonlinear shock parameter that indicates when the self-interaction of the probe due to the polarized vacuum becomes important and have shown that this can be consistently described using a probe-dependent vacuum refractive index.

As the shock parameter increases from zero, the spectrum of generated harmonics moves from an exponential decay to a power-law decay. The intensity of the jth harmonic in the shock regime was found in an all-order analytical solution and numerical simulation to be j^γ, where γ increases with propagation distance. A power-law behavior was observed for $-4.5 \lesssim \gamma \lesssim -2.4$, where the exponent is theoretically limited by $\gamma < -2$ as the probe pulse wave fronts would become infinitely steep and could no longer propagate. Due to the very high generated frequencies, the Heisenberg-Euler approach is no longer applicable at this point. Moreover, relaxation processes such as photon-seeded and Breit-Wheeler pair creation should then become probable.

When the polarization of the probe and background is parallel, all harmonics are generated in the parallel mode, but when the probe is perpendicularly polarized to the background, odd and even harmonics are split into probe and background polarization modes, respectively. Due to the birefringence of the vacuum, the probe polarization mode is generated more abundantly than in the background polarization mode. Moreover, due to the separation of frequencies, the parallel setup displays a sawtooth shock in the parallel mode, whereas the perpendicular setup displays a Kerr-like shock.

Both the simulational and analytical methods presented can be generalized to more complicated probe and background fields.

ACKNOWLEDGMENTS

P.B. acknowledges the very useful advice of A. Hindmarsh during development of the computational simulation. B.K. acknowledges the hospitality of H.R. and the Arnold Sommerfeld Center for Theoretical Physics at the Ludwig Maximilian University of Munich. This work was partially funded by Deutsche Forschungsgemeinschaft DFG under contracts FOR968, RU633/1-1, SFB-TR18 project B12 and EXC-158 (cluster of excellence MAP). Plots were generated with `Matplotlib` [95].

APPENDIX A: COEFFICIENTS FOR MODIFIED MAXWELL EQUATIONS

We define $\mathcal{L}_{xy} = \partial^2 \mathcal{L}_{\rm HE}/\partial x \partial y$ and $r^2 = a^2 + b^2$:

$$C_1 = 4\pi \frac{a\mathcal{L}_a - b\mathcal{L}_b}{r^2}, \tag{A1}$$

$$C_2 = \pi \frac{1}{r^6}[a(a^2-3b^2)\mathcal{L}_a + b(b^2-3a^2)\mathcal{L}_b - r^2(a^2\,\mathcal{L}_{aa} - 2ab\,\mathcal{L}_{ab} + b^2\mathcal{L}_{bb})], \tag{A2}$$

$$C_3 = \pi \frac{1}{r^6}[a(3b^2-a^2)\mathcal{L}_a + b(3a^2-b^2)\mathcal{L}_b - r^2(b^2\,\mathcal{L}_{aa} + 2ab\,\mathcal{L}_{ab} + a^2\,\mathcal{L}_{bb})], \tag{A3}$$

$$C_4 = \pi \frac{1}{r^6}\{b(3a^2-b^2)\mathcal{L}_a + a(a^2-3b^2)\mathcal{L}_b - r^2[ab\,\mathcal{L}_{aa} + (a^2-b^2)\,\mathcal{L}_{ab} - ab\,\mathcal{L}_{bb}]\}. \tag{A4}$$

For the first order (box diagram) and the second order (hexagon diagram) in the weak-field expansion, we find the following coefficients:

$$C_{1,\rm Box} = \frac{2\alpha}{45\pi}(E^2 - B^2), \quad C_{2,\rm Box} = -\frac{\alpha}{45\pi}, \tag{A5}$$

$$C_{3,\rm Box} = \tfrac{7}{4}C_{2,\rm Box}, \quad C_{4,\rm Box} = 0, \tag{A6}$$

$$C_{1,\rm Hex} = \frac{2\alpha}{315\pi}[6(E^2-B^2)^2 + 13(\mathbf{E}\cdot\mathbf{B})^2], \tag{A7}$$

$$C_{2,\rm Hex} = -\frac{4\alpha}{105\pi}(E^2 - B^2), \tag{A8}$$

$$C_{3,\rm Hex} = \tfrac{13}{24}C_{2,\rm Hex}, \tag{A9}$$

$$C_{4,\rm Hex} = -\frac{13\alpha}{315\pi}|(\mathbf{E}\cdot\mathbf{B})|. \tag{A10}$$

APPENDIX B: MATRIX FORM OF MODIFIED MAXWELL EQUATIONS

The modified Maxwell equations (5) and (6) can be written in matrix form:

$$(\mathbb{1}_4 + \mathbf{X})\partial_t \mathbf{f} + (\mathbf{Q} + \mathbf{Y})\partial_z \mathbf{f} = 0, \tag{B1}$$

where $\mathbf{f} = (E_x, E_y, B_x, B_y)^T$, $\mathbb{1}_4$ is the identity in four dimensions, $\mathbf{Q} = \mathrm{adiag}(1,-1,-1,1)$, and $\mathbf{X} = (x_{ij})$, $\mathbf{Y} = (y_{ij})$ are the vacuum perturbation, where the nonzero elements are given by

$$\begin{aligned}
x_{11} &= C_1 - C_2\rho_{11} - C_3\rho_{33} - 2C_4\rho_{13},\\
x_{12} &= -C_2\rho_{12} - C_3\rho_{34} - C_4(\rho_{14}+\rho_{23}),\\
x_{13} &= (C_2 - C_3)\rho_{13} + C_4(\rho_{33} - \rho_{11}),\\
x_{14} &= C_2\rho_{14} - C_3\rho_{23} + C_4(\rho_{34} - \rho_{12}),\\
x_{21} &= -C_2\rho_{12} - C_3\rho_{34} - C_4(\rho_{14}+\rho_{23}),\\
x_{22} &= C_1 - C_2\rho_{22} - C_3\rho_{44} - 2C_4\rho_{24},\\
x_{23} &= C_2\rho_{23} - C_3\rho_{14} + C_4(\rho_{34} - \rho_{12}),\\
x_{24} &= (C_2 - C_3)\rho_{24} + C_4(\rho_{44} - \rho_{22}),\\
y_{11} &= -C_2\rho_{14} + C_3\rho_{23} + C_4(\rho_{12} - \rho_{34}),\\
y_{12} &= -(C_2 - C_3)\rho_{24} + C_4(\rho_{22} - \rho_{44}),\\
y_{13} &= C_2\rho_{34} + C_3\rho_{12} - C_4(\rho_{14}+\rho_{23}),\\
y_{14} &= C_1 + C_2\rho_{44} + C_3\rho_{22} - 2C_4\rho_{24},\\
y_{21} &= (C_2 - C_3)\rho_{13} + C_4(\rho_{33} - \rho_{11}),\\
y_{22} &= C_2\rho_{23} - C_3\rho_{14} + C_4(\rho_{34} - \rho_{12}),\\
y_{23} &= -C_1 - C_2\rho_{33} - C_3\rho_{11} + 2C_4\rho_{13},\\
y_{24} &= -C_2\rho_{34} - C_3\rho_{12} + C_4(\rho_{14}+\rho_{23}),
\end{aligned}$$

where we define $\rho_{ij} := 4 f_i f_j$, such that, e.g., $\rho_{14} = 4E_x B_y$.

APPENDIX C: BIASED FINITE DIFFERENCES

The action of the matrix $\mathbf{D}$ on the vector $\tilde{\mathbf{u}}$ can be encoded in the use of an adaption of the DSS020 function from [46]

$$\mathbf{D}\tilde{\mathbf{u}} = \begin{pmatrix} d_-(u_1^1)\\ d_-(u_2^1)\\ d_+(u_3^1)\\ d_+(u_4^1)\\ d_-(u_1^2)\\ d_-(u_2^2)\\ d_+(u_3^2)\\ d_+(u_4^2)\\ \vdots \end{pmatrix},$$

where the function $d_-(u^l)$ is defined as

$$
\begin{aligned}
&d_-(u^l) := \\
&\quad l = 1: \\
&\qquad q(-25u^1 + 48u^2 - 36u^3 + 16u^4 - 3u^5), \\
&l = N-2: \\
&\qquad q(u^{N-4} - 8u^{N-3} + 8u^{N-1} - u^N), \\
&l = N-1: \\
&\qquad q(-u^{N-4} + 6u^{N-3} - 18u^{N-2} + 10u^{N-1} + 3u^N), \\
&\quad l = N: \\
&\qquad q(3u^{N-4} - 16u^{N-3} + 36u^{N-2} - 48u^{N-1} + 25u^N), \\
&\text{else} \\
&\qquad q(-3u^{l-1} - 10u^l + 18u^{l+1} - 6u^{l+2} + u^{l+3}),
\end{aligned}
$$

with $q = 1/12\Delta z$ and $d_+(u^l)$ as

$$
\begin{aligned}
&d_+(u^l) := \\
&\quad l = 1: \\
&\qquad q(-25u^1 + 48u^2 - 36u^3 + 16u^4 - 3u^5), \\
&\quad l = 2: \\
&\qquad q(-3u^1 - 10u^2 + 18u^3 - 6u^4 + u^5), \\
&\quad l = 3: \\
&\qquad q(u^1 - 8u^2 + 8u^4 - u^5), \\
&\quad l = N: \\
&\qquad q(3u^{N-4} - 16u^{N-3} + 36u^{N-2} - 48u^{N-1} + 25u^N), \\
&\text{else} \\
&\qquad q(-u^{l-3} + 6u^{l-2} - 18u^{l-1} + 10u^l + 3u^{l+1}).
\end{aligned}
$$

[1] F. Sauter, Z. Phys. **69**, 742 (1931).
[2] O. Halpern, Phys. Rep. **44**, 855 (1934).
[3] H. Euler and B. Kochel, Naturwissenschaften **23**, 246 (1935).
[4] V. Weisskopf, Kgl. Danske Videnskab. Selskab, Mat.-fys. Medd. **14**, 6 (1936).
[5] W. Heisenberg and H. Euler, Z. Phys. **98**, 714 (1936).
[6] J. Schwinger, Phys. Rev. **82**, 664 (1951).
[7] V. P. Gusynin and I. A. Shovkovy, Can. J. Phys. **74**, 282 (1996).
[8] V. P. Gusynin and I. A. Shovkovy, J. Math. Phys. **40**, 5406 (1999).
[9] G. V. Dunne and T. M. Hall, Phys. Rev. D **60**, 065002 (1999).
[10] H. Gies and L. Roessler, Phys. Rev. D **84**, 065035 (2011).
[11] M. Lutzky and J. S. Toll, Phys. Rep. **113**, 1649 (1959).
[12] N. N. Rozanov, Sov. Phys. JETP **76**, 991 (1993).
[13] V. V. Zheleznyakov and A. L. Fabrikant, Sov. Phys. JETP **55**, 794 (1982).
[14] J. S. Heyl and L. Hernquist, Phys. Rev. D **58**, 043005 (1998).
[15] J. S. Heyl and L. Hernquist, Phys. Rev. D **59**, 045005 (1999).
[16] Z. Bialynicka-Birula, Physica D **2**, 513 (1981).
[17] M. Marklund, P. K. Shukla, and B. Eliasson, Europhys. Lett. **70**, 327 (2005).
[18] N. B. Narozhny and A. M. Fedotov, Contemp. Phys. **56**, 249 (2015).
[19] P. A. Franken and J. F. Ward, Rev. Mod. Phys. **35**, 23 (1963).
[20] M. Marklund, Nat. Photon. **4**, 72 (2010).
[21] G. Rosen, Phys. Rep. **139**, A539 (1965).
[22] F. DeMartini, C. H. Townes, T. K. Gustafson, and P. L. Kelley, Phys. Rep. **164**, 312 (1967).
[23] D. Anderson and M. Lisak, Phys. Rev. A **27**, 1393 (1983).
[24] A. Di Piazza, K. Z. Hatsagortsyan, and C. H. Keitel, Phys. Rev. D **72**, 085005 (2005).
[25] A. M. Fedotov and N. B. Narozhny, Phys. Lett. A **362**, 1 (2006).
[26] E. Lundström, G. Brodin, J. Lundin, M. Marklund, R. Bingham, J. Collier, J. T. Mendonça, and P. Norreys, Phys. Rev. Lett. **96**, 083602 (2006).
[27] B. King and C. H. Keitel, New J. Phys. **14**, 103002 (2012).
[28] B. King, P. Böhl, and H. Ruhl, Phys. Rev. D **90**, 065018 (2014).
[29] H. Gies, F. Karbstein, and N. Seegert, New J. Phys. **15**, 083002 (2013).
[30] This corrects the extra factor of α in Eq. (4) from [28].
[31] R. Karplus and M. Neuman, Phys. Rev. **80**, 380 (1950).
[32] R. Wang, *Introduction to Orthogonal Transforms: With Applications in Data Processing and Analysis* (Cambridge University Press, Cambridge, 2012).
[33] B. King, H. Gies, and A. Di Piazza, Phys. Rev. D **86**, 125007 (2012).
[34] B. King, H. Gies, and A. Di Piazza, Phys. Rev. D **87**, 069905(E) (2013).
[35] A. Di Piazza, K. Z. Hatsagortsyan, and C. H. Keitel, Phys. Rev. Lett. **97**, 083603 (2006).
[36] S. L. Adler, Ann. Phys. **67**, 599 (1971).
[37] G. V. Dunne, in *Ian Kogan Memorial Collection, From Fields to Strings: Circumnavigating Theoretical Physics*, edited by M. Shifman *et al.* (World Scientific, Singapore, 2004), pp. 445–522.
[38] G. D. Mahan, *Applied Mathematics* (Springer Science+Business Media, New York, 2002).
[39] V. N. Gribov and J. Nyiri, *Quantum Electrodynamics* (Cambridge University Press, Cambridge, UK, 2001).
[40] I. Gradshteyn and I. Ryzhik, *Table of Integrals, Series, and Products* (Academic, San Diego, 2007).
[41] E. Fubini-Ghiron, Alta Frequenza **4**, 530 (1935).
[42] T. D. Rossing, *Springer Handbook of Acoustics* (Springer, New York, 2007).
[43] M. B. Carver, J. Comput. Phys. **35**, 57 (1980).
[44] A. C. Hindmarsh, P. N. Brown, K. E. Grant, S. L. Lee, R. Serban, D. E. Shumaker, and C. S. Woodward, ACM Trans. Math. Softw. **31**, 363 (2005).
[45] J. C. Strikwerda, *Finite Difference Schemes and Partial Differential Equations* (SIAM, Singapore, 2004).
[46] W. E. Schiesser, *The Numerical Method of Lines Integration of Partial Differential Equations* (Academic, San Diego, 1991), Vol. 17.
[47] P. Lancaster and M. Tismenetsky, *The Theory of Matrices: With Applications* (Academic, New York, 1985).

[48] G. H. Golub and C. F. Van Loan, *Matrix Computations* (JHU, Baltimore, 2012), Vol. 3.
[49] I. Wolfram Research, *Mathematica* (Wolfram Research, Champaign, IL, 2012), version 9.0 ed.
[50] R. Baier and P. Breitenlohner, Nuovo Cim. B **47**, 117 (1967).
[51] W. Dittrich and H. Gies, *Probing the Quantum Vacuum* (Springer, Berlin, 2000).
[52] S. Meuren, K. Z. Hatsagortsyan, C. H. Keitel, and A. Di Piazza, Phys. Rev. D **91**, 013009 (2015).
[53] G. B. Arfken, H. J. Weber, and F. E. Harris, *Mathematical Methods for Physicists*, 7th ed. (Elsevier, Amsterdam, 2012).
[54] G. N. Watson, *Theory of Bessel Functions* (Cambridge University Press, Cambridge, 1922).
[55] S. B. P. Radnor, L. E. Chipperfield, P. Kinsler, and G. H. C. New, Phys. Rev. A **77**, 033806 (2008).
[56] P. Kinsler, S. B. P. Radnor, J. C. A. Tyrrell, and G. H. C. New, Phys. Rev. E **75**, 066603 (2007).
[57] P. McKenna, D. Neely, R. Bingham, and D. A. Jaroszynski, *Laser-Plasma Interactions and Applications* (Springer, Berlin, 2013).
[58] W. P. Leemans *et al.*, Phys. Rev. Lett. **113**, 245002 (2014).
[59] B. King, Phys. Rev. A **91**, 033415 (2015).
[60] R. Lichters, J. Meyer-ter-Vehn, and A. Pukhov, Phys. Plasmas **3**, 3425 (1996).
[61] S. Gordienko, A. Pukhov, O. Shorokhov, and T. Baeva, Phys. Rev. Lett. **93**, 115002 (2004).
[62] T. Baeva, S. Gordienko, and A. Pukhov, Phys. Rev. E **74**, 046404 (2006).
[63] P. A. Norreys, M. Zepf, S. Moustaizis, A. P. Fews, J. Zhang, P. Lee, M. Bakarezos, C. N. Danson, A. Dyson, P. Gibbon *et al.*, Phys. Rev. Lett. **76**, 1832 (1996).
[64] H. R. Reiss, J. Math. Phys. **3**, 59 (1962).
[65] A. I. Nikishov and V. I. Ritus, Sov. Phys. JETP **19**, 529 (1964).
[66] G. Breit and J. A. Wheeler, Phys. Rep. **46**, 1087 (1934).
[67] O. Pike, F. Mackenroth, E. Hill, and S. Rose, Nat. Photon. **8**, 434 (2014).
[68] C. Winterfeldt, C. Spielmann, and G. Gerber, Rev. Mod. Phys. **80**, 117 (2008).
[69] L. Levi, *Applied Optics* (John Wiley and Sons, New York, 1968).
[70] P. C. Ferreira and J. D. de Deus, Eur. Phys. J. C **54**, 539 (2008).
[71] V. Yanovsky *et al.*, Opt. Express **16**, 2109 (2008).
[72] J. T. Mendonca *et al.*, Phys. Lett. A **359**, 700 (2006).
[73] T. Heinzl *et al.*, Opt. Commun. **267**, 318 (2006).
[74] A. Ferrando, H. Michinel, M. Seco, and D. Tommasini, Phys. Rev. Lett. **99**, 150404 (2007).
[75] D. Tommasini and H. Michinel, Phys. Rev. A **82**, 011803 (2010).
[76] B. King, A. D. Piazza, and C. H. Keitel, Nat. Photon. **4**, 92 (2010).
[77] B. King, A. Di Piazza, and C. H. Keitel, Phys. Rev. A **82**, 032114 (2010).
[78] G. Y. Kryuchkyan and K. Z. Hatsagortsyan, Phys. Rev. Lett. **107**, 053604 (2011).
[79] Y. Monden and R. Kodama, Phys. Rev. Lett. **107**, 073602 (2011).
[80] V. Dinu, T. Heinzl, A. Ilderton, M. Marklund, and G. Torgrimsson, Phys. Rev. D **89**, 125003 (2014).
[81] V. Dinu, T. Heinzl, A. Ilderton, M. Marklund, and G. Torgrimsson, Phys. Rev. D **90**, 045025 (2014).
[82] H. Hu and J. Huang, Phys. Rev. A **90**, 062111 (2014).
[83] F. Karbstein and R. Shaisultanov, Phys. Rev. D **91**, 085027 (2015).
[84] G. Brodin, M. Marklund, and L. Stenflo, Phys. Rev. Lett. **87**, 171801 (2001).
[85] H. Gies, F. Karbstein, and R. Shaisultanov, Phys. Rev. D **90**, 033007 (2014).
[86] M. Marklund and P. K. Shukla, Rev. Mod. Phys. **78**, 591 (2006).
[87] A. Di Piazza *et al.*, Rev. Mod. Phys. **84**, 1177 (2012).
[88] D. Bernard *et al.*, Eur. Phys. J. D **10**, 141 (2000).
[89] G. Zavattini, U. Gastaldi, R. Pengo, G. Ruoso, F. D. Valle, and E. Milotti, Int. J. Mod. Phys. A **27**, 1260017 (2012).
[90] A. Cadène, P. Berceau, M. Fouché, R. Battesti, and C. Rizzo, Eur. Phys. J. D **68**, 16 (2014).
[91] E. P. Mazets *et al.*, Nature (London) **282**, 587 (1979).
[92] C.-F. Chang, K. Cheung, and T.-C. Yuan, Astron. J. **392**, L9 (1992).
[93] W. C. G. Ho and D. Lai, Mon. Not. R. Astron. Soc. **338**, 233 (2003).
[94] A. K. Harding and D. Lai, Rep. Prog. Phys. **69**, 2631 (2006).
[95] J. D. Hunter, Comput. Scie. Eng. **9**, 90 (2007).